Three Dimensional Laser Diagnostics for Turbulent Flows and Flames

Wenjiang Xu

Dissertation submitted to the faculty of the Virginia Polytechnic Institute and State University in partial fulfillment of the requirements for the degree of

Doctor of Philosophy

In

Aerospace Engineering

Lin Ma, Chair

K. Todd Lowe

Michael L. Philen

Heng Xiao

Sep 29, 2017

Blacksburg, Virginia

Keywords: Optical diagnostics, Tomography, Laser induced fluorescence

Three Dimensional Laser Diagnostics for Turbulent Flows and Flames

Wenjiang Xu

ABSTRACT

Due to their scientific significance and practical applications, turbulent flows and flames have been under extensive and intensive research for a long time. Turbulent flows and flames of interests to practice inherently have three-dimensional (3D) spatial structures, and therefore diagnostic techniques that can instantaneously resolve their 3D spatial features have long been desired and probably are needed to ultimately answer some of the open research questions. The goal of this dissertation thus is to investigate such diagnostics and demonstrate their capability and limitations in a range of turbulent flows/flames. To accomplish this goal, this dissertation developed and evaluated the following three diagnostic methods: tomographic chemiluminescence (TC), volumetric laser induced fluorescence (VLIF), and super-resolution planar laser induced fluorescence (SR-PLIF).

First, 3D flame topography of well-controlled laboratory flames was measured with TC method and validated by a simultaneous 2D Mie scattering measurement. The results showed that the flame topography obtained from TC and the Mie scattering agreed qualitatively, but quantitative difference on the order of millimeter was observed between these two methods. Such difference was caused by the limitations of the TC method. The first limitation involves TC's reliance on chemiluminescence of nascent radicals (mainly CH*) in reacting flows, causing ambiguity in the definition of flame front and limiting its applications to certain

types of reactive flow only. The second limitation involves TC's inability to study an isolated region of interest because the chemiluminescence is emitted everywhere in the flame.

Based on the above understanding of the TC technique, the second part of this dissertation studied a VLIF method to overcome the above limitations of the TC technique. Compared with the TC technique, the VLIF method can be used in either reacting or non-reacting flow and on any particular region of interest. In the VLIF technique, the fluorescence signal was generated by exciting a target species with a laser slab of certain thickness. The signal was recorded by cameras from different perspectives, and then a VLIF tomographic algorithm was applied to resolve the spatial distribution of the concentration of the target species. An innovative 3D VLIF algorithm was proposed and validated by well-designed experiment. This model enables analysis of VLIF performance in terms of signal level, size of the field of view in 3D, and accuracy. However, due to the limited number of views and the tomographic reconstruction itself, the spatial resolution of VLIF methods is limited.

Hence, the third part of this dissertation investigated a SR-PLIF method to provide a strategy to improve the spatial resolution in two spatial directions, and also to extend the measurement range of scanning 3D imaging strategies. The SR-PLIF method used planar images captured simultaneously from two (or more) orientations to reconstruct a final image with resolution enhanced or blurring removed. Both the development of SR algorithm, and the experimental demonstration of the SR-PLIF method were reported.

Three Dimensional Laser Diagnostics for Turbulent Flows and Flames

Wenjiang Xu

General Audience Abstract

Optical diagnostics have become indispensable tools for the study of the turbulent flows and flames. Due to the inherently 3D structure of turbulent flows and flames, diagnostic techniques which can provide 3D measurements have been long desired. Therefore, this dissertation reports the development of three optics diagnostic methods that can provide such measurement capability, with a detailed discussion of their capabilities and limitations. The methods studied are tomographic chemiluminescence (TC), volumetric laser-induced fluorescence (VLIF), and super-resolution planar laser induced fluorescence (SR-PLIF). For the TC technique, the emission of light from combustion radicals (CH* and OH*) was recorded by multiple cameras placed at different orientations. A numerical algorithm was then applied to reconstruct the 3D flame structure. For the VLIF technique, a laser slab was used to excite a specific chemical species in the flame, which were captured from different perspectives to reconstruct the flow or flame structure in 3D. For the SR-PLIF technique, a series of planar images were recorded from multiple orientations to reconstruct a target image with higher resolution or to extend the measurement volume of scanning 3D diagnostics.

It is expected that the results obtained in this dissertation lay the groundwork for further development and expanded application of 3D diagnostics for the study of turbulent flows and combustion processes.

Acknowledgement

After the past several years of PhD study, I am so glad that I am now standing at the finish line. Graduate study has been really a struggling for me, until I restarted a new track three years ago with Dr. Lin Ma.

I own my deepest gratitude to my advisor at Virginia Tech, Professor Lin Ma. It would be impossible for me to accomplish this dissertation and my Ph.D. career without his consistent help and support. Dr. Ma pulled me back from the wrong track, and taught me not only how to do research but also how to survive and thrive in graduate school. I also would like to thank Dr. Todd Lowe, Dr. Heng Xiao, and Dr. Michael Philen for serving on my committee and providing me academic and professional advice.

I would like to extend my thanks to my colleagues and friends in AOE. They are Fan He, Yue Wu, Qingchun Lei, Haoting Wang, Ning Liu, Di Zhang, Ken Brown, A. J. Wickersham, and many others. I would like to also thank all the friends I got to know with luck in the Town of Blacksburg. Because of all of you, the life in this small town was not so tedious.

My greatest gratitude goes to my families, for their love and supports which helped me go through all the difficult time.

Table of Contents

List of Figures

Chapter 1 Introduction

Turbulent flow/combustion is of profound scientific significance and wide engineering applications in many engineering devices that provide the majority of our energy [1-3]. Therefore, turbulent flows/combustion have been studied extensively for many decades. Although much progress has already been made and many different tools have been developed, there still exists many unresolved questions. Notably, due to the inherent 3D (three-dimensional) structures of turbulent flows and flames, it has been long desired to have experimental techniques that can resolve flow and flame structures in all three spatial directions. The goal of this dissertation thus is to investigate such diagnostics and demonstrate their capability and limitations in a range of turbulent flows/flames.

Overview of optical diagnostics

Previous researchers have developed many tools to experimentally measure flame structures. Traditionally, Pitot tube, hotwire, thermocouple, and oil smoke have all been used to study turbulent flow characteristics. Continued advancements in laser technologies (especially high pulse energy lasers), electronics, cameras (especially high-speed cameras), and other optical devices have enabled the development of non-intrusive optic diagnostics. During the past a few decades, non-intrusive diagnostics have been demonstrated as powerful and indispensable tools for the study of turbulent flows/combustion [4, 5].

Compared with traditional techniques such as Pitot tubes or thermocouples, optical diagnostic methods offer several key advantages. First, optical diagnostics are non-intrusive and do not cause disturbance onto the test section. Second, since optical

diagnostics do not require direct interaction with the test medium, they can allow measurement in harsh environments involving high temperature, high pressure, and corrosive species [6]. Lastly, optical diagnostics also provide promising perspectives for remote control and implementation, which is a key enabling technology for future data-driven devices and systems.

Despite of the above mentioned advantages, optical diagnostics also have limitations and should be carefully evaluated in practical applications. First, optical access is always a concern for the application of optical diagnostics in practice, since most engineering devices are operated in constrained spaces without or with limited optical access. Second, post processing of the raw data (such as 2D images) is typically required to obtain the target property, and the physics involved in the post processing is often not trivial. For example, interpretation of LIF signal usually requires a good knowledge on the modeling of LIF mechanism and a good estimate of the quenching rates [7, 8], which are difficult to obtain except in some simplified systems. Third, the cost of performing optical diagnostics is usually expensive, especially when high-energy laser(s), intensifier(s), and high-speed camera(s) are used in the experiment. Nevertheless, continued advancements in material optics, electronics, fiber technology, et al should facilitate the applications of optical diagnostics, and reduce the implementation difficulty and cost.

Past efforts have developed a variety of optics diagnostic techniques to measure a range of key flows/combustion properties. Notable examples include Mie scattering [9, 10], Rayleigh scattering [11], laser induced fluorescence (LIF) [12-14], Raman scattering [5, 15], particle imaging velocimetry [16], laser Doppler velocimetry [17], chemiluminescence [18, 19] and so on. These techniques are developed to measure

different flow/flame properties, and each of them typically provides optical performance under certain circumstances. For example, although Raman technique is an excellent choice to measure multiple major species in combustion [5], such as CH_4, O_2, H_2O, CO_2, and N_2, its weak signal level limits its usage in the measurement of minor species such as CH. As another example, PIV is a mature technique developed for measuring the velocity field in turbulent flows, but the seeding required in PIV may interfere with other measurements and therefore limits the application of PIV. To obtain complete information of turbulent flows and flames, multi-scalar and or multi-vector filed measurements are highly desired and intensive research efforts have been invested. For example, one of these efforts involves an implementation of simultaneous PIV and PLIF measurements in turbulent combustion [20, 21] to measure a combustion species distribution and velocity fields.

Among all the diagnostics reviewed above, the primary diagnostic concepts involved in this dissertation are chemiluminescence and laser-induced fluorescence (LIF). The following sections provides more details and in-depth discussion of these diagnostic concepts and motivate their extension to 3D measurements using tomographic chemiluminescence (TC) and volumetric laser-induced fluorescence (VLIF).

3D tomographic chemiluminescence

Diagnostics based on chemiluminescence uses the photons emitted from excited radicals generated by chemical reactions in flames, such as CH* and/or OH*. The nascent emission from these excited radicals provides the signal, therefore eliminating the need for laser illumination and simplifying the experimental setup. However, reliance on nascent flame emission causes ambiguities in the measurement spatial resolution because

the image formed on a camera is the result of line-of-sight integration. Past work has demonstrated that tomographic chemiluminescence (TC) represents an effective way of overcoming this limitation and enabling spatially-resolved flame front measurements based on chemiluminescence signal. The TC approach involves using multiple cameras to image the target flame from multiple orientations. The line-of-sight integrated emission images captured by these cameras (termed projections) are then used as inputs in a tomographic algorithm to reconstruct the 3D flame structures. In TC measurement, although the hardware implementation is relative simple, the post-processing of the 2D images and tomographic reconstruction is not trivial.

With the advancement of camera and computational algorithm, recent work has demonstrated the feasibility of using TC technique to conduct instantaneous 3D flame measurements [19, 22-26]. The measurements with temporal resolution above multi-kHz [27] and spatial resolution below millimeter, in a volume with dimension on the order of decimeter, have been demonstrated. These past efforts illustrate the advantages and capabilities of the TC technique and motivate further research [26]. One of the key research needs for the further development of the TC technique involves the validation of the 3D measurements (a research need shared also by other tomographic-based 3D diagnostics). Several methods have been developed and applied in these past research efforts for validation purposes, including numerical simulations based on phantoms [19, 22, 24, 28], use of controlled flames with known patterns [19, 23, 29], and comparison between 3D results obtained experimentally and simulated results obtained via ray-tracing [30, 31]. Further validation is always desired for the development of new diagnostic tools, and the validation method should ideally be as direct as possible.

Therefore, Chapter 2 of this dissertation describes an additional validation method by a direct comparison between the 3D TC measurements and 2D Mie scattering measurements. Specifically, measurements of flame topography were performed on several target flames by the TC and planar Mie scattering techniques simultaneously. The TC measurements provided 3D topography and the Mie scattering measurements provided a 2D cross-section of the 3D topography across the plane illuminated by the laser sheet. The 2D cross-sectional Mie measurements were then directly compared to the 3D measurements at the illuminated plane for validation purposes. Such comparison is also expected to be useful beyond the validation of 3D measurements, because both chemiluminescence and Mie scattering techniques are extensively applied for flame visualization.

3D laser induced fluorescence

Laser-induced fluorescence (LIF) enables researchers to obtain a variety of key flow/combustion parameters, ranging from species concentration [7, 8, 32], temperature [33], reaction progress [34], and mixture fraction [35]. In the past, LIF-based diagnostics have been largely established for measurements at a point, alone a line, or across a plane via PLIF (planar LIF) [12]. Most practical flows are turbulent and therefore inherently three-dimensional (3D) in space and dynamic in time [5, 36]. Therefore, there is a strong motivation to extend LIF to instantaneous 3D measurements.

Compared with the TC approach, LIF-based diagnostic method presents some key advantages. First, since the LIF signal is emitted from radicals excited by the laser, only the illuminated portion of the flow will be imaged. This allows an obvious advantage that one can only study the interested portion of the flow, such as the central plane of the

flow. Second, since the LIF signal is generated only when the laser pulse is on, the flow structure can be 'frozen' in a small period of time when the laser is on, effectively enhancing the temporal resolution of the measurements. Using LIF techniques, measurements time on the order of nanoseconds or shorter are routinely accomplished. Third, the LIF technique can be applied on either nascent radicals [37, 38] (such as CH, OH, CH_2O), or seeded species [12, 14] (such as I_2 molecule), and therefore enables measurements not only in reactive flows but also non-reacting flows. Because of these advantages, the second part of this dissertation studies LIF-based 3D optical diagnostics to overcome the limitations of chemiluminescence-based diagnostics as described above.

Two different LIF-based methods for 3D optical diagnostics have been studied. The first strategy involves combining tomography with LIF [39-46]. In this method, 3D LIF signal is generated volumetrically by expanding the laser beam to fill a target volume (and correspondingly this approach is termed VLIF, volumetric LIF). The volumetric LIF signal is projected and measured by cameras placed at different locations, and these projections are then used as the inputs to a tomography algorithm to reconstruct the 3D distribution of the target species. Recently, a variety of demonstration work of VLIF has been reported under various circumstances, such as cold jet flow with seeded species [39, 41], flame topography measurement based on nascent radicals (e.g. CH) [47, 48], soot volume fraction measurement [39] and so on. To date, therefore, the feasibility of VLIF technique has already been successfully demonstrated, with high temporal resolution [49] and spatial resolution in all directions [48]. However, the fundamental numerical model of VLIF, capabilities and limitations of VLIF technique [37], and the reliance of VLIF on laser slab thickness and pulse energy has not been studied yet. And it is the goal of this

dissertation to address some of these issues.

The second possible strategy to enable 3D LIF involves a *scanning PLIF method* [50-56]. With this approach, one scans the probe laser sheet rapidly across multiple spatial locations and then records PLIF images sequentially at these locations, which are eventually compiled to form a 3D measurement. A practical problem in this technique is that the scanning range of the laser sheet is limited, which restrict PLIF's capability and applicability. Also, blurring can occur due to a variety of reasons which further deteriorate the resolution of the PLIF measurements, such as misalignment of the excitation laser sheet and the focal plane of the camera, mechanical vibration or movement of the experimental rig, and the also the scanning of the laser sheet to obtain PLIF measurements at multiple spatial locations [57, 58]. A straightforward and commonly practiced method to mitigate the blurring issue involves using a small aperture to increase the depth of field (DOF) of the imaging systems. This straightforward approach however is practiced at the cost of signal level, which approximately scales to the second power of the aperture [59]. Therefore, it is the goal of this dissertation to investigate an alternative strategy to expand the capabilities of scanning three-dimensional LIF measurements. To accomplish this goal, this dissertation developed a super-resolution LIF technique that can either improve the spatial resolution in a plane significantly, or to extend the measurement region significantly without blurring or loss of spatial resolution.

Contributions and organization of the dissertation

Based on the above understanding of past efforts and the research needs for 3D optical

diagnostics, the main contributions of this dissertation contributes to optical diagnostics can be summarized into the following three aspects:

- This work developed a measurement technique named 3D TC, applied it to measure flame topography of various lab-scale flames, and validated the measurements using direct Mie scattering measurement of a 2D slice of the 3D topography.
- This work developed and validated a novel 3D VLIF algorithm for flame topography measurement, enabling the capability to analyze VLIF performance in terms of signal level, size of the field of view in 3D, and accuracy.
- This work developed and demonstrated an effective SR-PLIF method to improve the spatial resolution or to extend the measurement volume of 3D diagnostics.

This dissertation follows the manuscript format and the rest of this dissertation is divided into several self-contained chapters. Each subsequent chapter is a published paper or a manuscript submitted to a peer-reviewed journal.

Chapter 2 is a published paper, entitled "3D flame topography obtained by tomographic chemiluminescence with direct comparison to planar Mie scattering measurement". It is published in Applied Optics, 54 (2015) 2174-2182 [18]. This paper discusses the experimental validation of the 3D TC diagnostics using well controlled laboratory scale flames. The focus is to directly and quantitatively validate the TC result of flame topography by comparing it against simultaneous planar measurements obtained from Mie scattering technique. Since the Mie scattering signal is generated by a planar laser sheet, the comparison was performed by overlapping the Mie scattering image of the flame front on 2D reconstructed slices of TC. It can be concluded from the comparison that the accuracy of the TC technique on flame topography measurement was

on the order of millimeter. Because the TC method uses nascent emission of radicals (CH*) produced by combustion reactions if, it can only be applied in reacting flows. Moreover, the signal is emitted volumetrically from everywhere of the flame and currently there is no effective way to isolate the chemiluminescence from any particular region, prohibiting TC's application to study an isolated part of interest. Since the entire flame has to be captured, the spatial resolution of the TC method is limited when the number of cameras are fixed. Therefore, the second part of this dissertation investigated a VLIF method to overcome these limitations of the TC technique.

Chapter 3 is a published paper, entitled "Analysis of 3D combustion measurements using CH-based tomographic VLIF (volumetric laser induced fluorescence". It is published in Combustion and Flame 182 (2017) 179-189. This paper presents an innovative VLIF algorithm based on the CH $C^2\Sigma^+$-- $X^2\Pi(0,0)$ LIF transition. Although the model was based on CH transition, the results obtained should be also useful for other species. The accuracy of the 3D VLIF was validated by comparing the mean signal level of model simulation with experimental data and then examined further through a series of numerical simulations. In the VLIF method, the fluorescence signal is generated by a laser slab with a certain thickness (ranging from several millimeter to a few centimeters in this work) and is recorded by cameras from different perspectives. Then a VLIF tomographic reconstruction algorithm is applied to resolve the spatial distribution of the flame/flow structure. Compared with the TC technique, the VLIF technique can be applied on both reacting or non-reacting flows, and on any special region of interest in the flow (by shaping and aligning the excitation laser slab). Not only the distribution of the radical CH, but also many other species (such as CH2O) and temperature field can

also potentially be measured or inferred from the PLIF measurements. This work also I identified one of the limitations of the VLIF technique: its limited spatial resolution in a given measurement volume (or vice versa, its limited measurement volume at a given level of spatial resolution) due to the limited views used in practice. Therefore, the next part of this dissertation investigated methods to enhance the spatial resolution or the measurement volume of three-dimensional measurements.

Chapter 4 is a manuscript under review, entitled "Super resolution PLIF demonstrated in turbulent jet flows seeded with I_2". The manuscript has been submitted to Optics and Laser Technology and is currently under review. This manuscript reports the development of a SR-PLIF method, and its demonstration on turbulent nitrogen jet flows seeded with I_2 molecules. The SR-PLIF method uses PLIF images captured simultaneously from two (or more) orientations to reconstruct a final PLIF image with resolution enhanced or blurring removed. This method is useful in two ways for imaging diagnostics. First, it is useful when high resolution flow details in a particular plane is desired, while the high resolution in all three directions is difficult to achieve. Second, it is useful to extend the measurement volume of scanning 3D diagnostics. An issue with scanning 3D diagnostics is that when the laser sheet scans out of the focal-depth of the imaging system, the images become blurred. The SR-PLIF method can overcome this limitation and extends the measurement range of the 3D scanning techniques. Using controlled samples with two cameras, the spatial resolution in the best case was improved from 1.3 mm in the projections to 0.04 mm in the SR image, in terms of the spreading width of a sharp edge. With turbulent flows, an image sharpness measure was developed to quantify the spatial resolution, and SR reconstruction with two cameras can improve

the spatial resolution by ~2× compared to the projections in terms of the sharpness measure.

Finally, Chapter 5 summarizes the dissertation and suggests several future research directions.

References

1. Peters, N., *Turbulent combustion*. 2000: Cambridge university press.

2. Glassman, I., Yetter, R.A., and Glumac, N.G., *Combustion*. 2014: Academic press.

3. Clavin, P., *Dynamic behavior of premixed flame fronts in laminar and turbulent flows.* Progress in Energy and Combustion Science, 1985. **11**(1): p. 1-59.

4. Eckbreth, A.C., *Laser diagnostics for combustion temperature and species*. Vol. 3. 1996: CRC Press.

5. Barlow, R.S., *Laser diagnostics and their interplay with computations to understand turbulent combustion* Proceedings of the Combustion Institute 2007. **31**(1): p. 49-75.

6. Kohse-Höinghaus, K., Barlow, R.S., Aldén, M., and Wolfrum, J., *Combustion at the focus: laser diagnostics and control.* Proceedings of the Combustion Institute, 2005. **30**(1): p. 89-123.

7. Berg, P.A., Hill, D.A., Noble, A.R., Smith, G.P., Jeffries, J.B., and Crosley, D.R., *Absolute CH concentration measurements in low-pressure methane flames: Comparisons with model results.* Combustion and flame, 2000. **121**(1): p. 223-235.

8. Luque, J. and Crosley, D., *Absolute CH concentrations in low-pressure flames measured with laser-induced fluorescence.* Applied Physics B, 1996. **63**(1): p. 91-98.

9. Sun, X., Li, X., and Ma, L., *A closed-form method for calculating the angular distribution of multiply scattered photons through isotropic turbid slabs.* Optics express, 2011. **19**(24): p. 23932-23937.

10. Ma, L., Wu, Y., Lei, Q., Xu, W., and Carter, C.D., *3D flame topography and curvature measurements at 5 kHz on a premixed turbulent Bunsen flame.* Combustion and Flame, 2016. **166**: p. 66-75.

11. Wang, F., Sfeir, M.Y., Huang, L., Huang, X.H., Wu, Y., Kim, J., Hone, J., O'Brien, S., Brus, L.E., and Heinz, T.F., *Interactions between individual carbon nanotubes studied by Rayleigh scattering spectroscopy.* Physical review letters, 2006. **96**(16): p. 167401.

12. Hanson, R., Seitzman, J., and Paul, P., *Planar laser-fluorescence imaging of combustion gases.* Applied Physics B, 1990. **50**(6): p. 441-454.

13. Hiller, B. and Hanson, R., *Properties of the iodine molecule relevant to laser-induced fluorescence experiments in gas flows.* Experiments in Fluids, 1990. **10**(1): p. 1-11.

14. Lozano, A., Yip, B., and Hanson, R.K., *Acetone: a tracer for concentration measurements in gaseous flows by planar laser-induced fluorescence.* Experiments in Fluids, 1992. **13**(6): p. 369-376.

15. Zumbusch, A., Holtom, G.R., and Xie, X.S., *Three-dimensional vibrational imaging by coherent anti-Stokes Raman scattering.* Physical review letters, 1999. **82**(20): p. 4142.

16. Adrian, R.J., *Particle-imaging techniques for experimental fluid mechanics.* Annual review of fluid mechanics, 1991. **23**(1): p. 261-304.

17. Lyn, D., Einav, S., Rodi, W., and Park, J.-H., *A laser-Doppler velocimetry study of ensemble-averaged characteristics of the turbulent near wake of a square cylinder.* Journal of Fluid Mechanics, 1995. **304**: p. 285-319.

18. Xu, W., Wickersham, A.J., Wu, Y., He, F., and Ma, L., *3D flame topography obtained by tomographic chemiluminescence with direct comparison to planar Mie scattering measurements.* Applied Optics, 2015. **54**(9): p. 2174-2182.

19. Cai, W., Li, X., Li, F., and Ma, L., *Numerical and experimental validation of a three-dimensional combustion diagnostic based on tomographic chemiluminescence.* Optics Express, 2013. **21**(6): p. 7050-7064.

20. Su, L. and Mungal, M., *Simultaneous measurements of velocity and scalar fields: application in crossflowing jets and lifted jet diffusion flames.* Ann Res Briefs, 1999: p. 19-36.

21. Boxx, I., Heeger, C., Gordon, R., Böhm, B., Aigner, M., Dreizler, A., and Meier, W., *Simultaneous three-component PIV/OH-PLIF measurements of a turbulent lifted, C 3 H 8-Argon jet diffusion flame at 1.5 kHz repetition rate.* Proceedings of the Combustion Institute, 2009. **32**(1): p. 905-912.

22. Floyd, J., Geipel, P., and Kempf, A.M., *Computed Tomography of Chemiluminescence (CTC): Instantaneous 3D measurements and Phantom studies of a turbulent opposed jet flame.* Combust. Flame, 2011. **158**(2): p. 376-391.

23. Floyd, J. and Kempf, A.M., *Computed Tomography of Chemiluminescence (CTC): High resolution and instantaneous 3-D measurements of a Matrix burner.* Proc. Combust. Inst., 2011. **33**: p. 751-758.

24. Denisova, N., Tretyakov, P., and Tupikin, A., *Emission tomography in flame diagnostics.* Combustion and Flame, 2013. **160**(3): p. 577-588.

25. Li, X. and Ma, L., *Volumetric imaging of turbulent reactive flows at kHz based on computed tomography.* Optics Express, 2014. **22**(4): p. 4768-4778.

26. Li, X. and Ma, L., *Capabilities and limitations of 3D flame measurements based on computed tomography of chemiluminescence.* Combustion and Flame, 2014. **in press**.

27. Wu, Y., Lei, Q., and Ma, L., *Experimental demonstration of 4D imaging in two-phase flows based on computed tomography at 5 kHz.* APPLIED OPTICS, 2014. **53**(24): p. 5547-5553.

28. Cai, W., Li, X., and Ma, L., *Practical aspects of implementing three-dimensional tomography inversion for volumetric flame imaging.* Applied Optics, 2013. **52**(33): p. 8106-8116.

29. MinWook Kang, Y.W., Lin Ma, *Fiber-Based Endoscopes for 3D Combustion Measurements:View Registration and Spatial Resolution.* Combustion and Flame, 2014. **16**(12): p. 3063–3072.

30. Zhao, Y., Li, X., and Ma, L., *Multidimensional Monte Carlo model for two-photon laser-induced fluorescence and amplified spontaneous emission.* COMPUTER PHYSICS COMMUNICATIONS, 2012. **183**(8): p. 1588-1595.

31. Li, X. and Ma, L., *Three-Dimensional Measurements of Turbulent Jet Flames at kHz Rate Based on Tomographic Chemiluminescence* in *AIAA SciTech 2014, Paper AIAA-2014-0735*. 2014: National Harbor, MD.

32. Kristensson, E., Li, Z., Berrocal, E., Richter, M., and Aldén, M., *Instantaneous 3D imaging of flame species using coded laser illumination.* Proceedings of the Combustion Institute.

33. Seitzman, J.M., Kychakoff, G., and Hanson, R.K., *Instantaneous temperature field measurements using planar laser-induced fluorescence.* Optics Letters, 1985. **10**(9): p. 439-441.

34. Tanahashi, M., Murakami, S., Choi, G.-M., Fukuchi, Y., and Miyauchi, T., *Simultaneous CH–OH PLIF and stereoscopic PIV measurements of turbulent premixed flames.* Proceedings of the Combustion Institute, 2005. **30**(1): p. 1665-1672.

35. Zhao, Y., Tong, C., and Ma, L., *Demonstration of a New Laser Diagnostic Based on Photodissociation Spectroscopy for Imaging Mixture Fraction in a Non-premixed Jet Flame.* Applied Spectroscopy, 2010. **64**(4): p. 377-383.

36. Nathan, G., Kalt, P., Alwahabi, Z., Dally, B., Medwell, P., and Chan, Q., *Recent advances in the measurement of strongly radiating, turbulent reacting flows.* Progress in Energy and Combustion Science, 2012. **38**(1): p. 41-61.

37. Xu, W., Carter, C.D., Hammack, S.D., and Ma, L., *Analysis of 3D combustion measurements using CH-based tomographic VLIF (volumetric laser induced fluorescence).* Combustion and Flame (in production), 2017.

38. Skiba, A.W., Wabel, T.M., Carter, C.D., Hammack, S.D., Temme, J.E., Lee, T., and Driscoll, J.F., *Reaction layer visualization: A comparison of two PLIF techniques and advantages of kHz-imaging.* Proceedings of the Combustion Institute, 2017. **36**(3): p. 4593-4601.

39. Halls, B.R., Thul, D.J., Michaelis, D., Roy, S., Meyer, T.R., and Gord, J.R., *Single-shot, volumetrically illuminated, three-dimensional, tomographic laser-induced-fluorescence imaging in a gaseous free jet.* Optics Express, 2016. **24**(9): p. 10040-10049.

40. Ma, L., Lei, Q., Ikeda, J., Xu, W., Wu, Y., and Carter, C.D., *Single-shot 3D flame diagnostic based on volumetric laser induced fluorescence (VLIF).* Proceedings of the Combustion Institute, 2017. **36**(3): p. 8.

41. Wu, Y., Xu, W., Lei, Q., and Ma, L., *Single-shot volumetric laser induced fluorescence (VLIF) measurements in turbulent flows seeded with iodine.* Optics Express, 2015. **23**(26): p. 33408-33418.

42. Benjamin, R.H., James, R.G., Naibo, J., Mikhail, S., Sukesh, R., and Terrence, R.M., *High-speed three-dimensional tomographic measurements for combustion systems*, in *32nd AIAA Aerodynamic Measurement Technology and Ground Testing Conference*. 2016, American Institute of Aeronautics and Astronautics.

43. Ma, L., Xu, W., Lei, Q., Ikeda, J., and Carter, C., *Single-Shot 3D Flame Imaging Using CH-Based VLIF (Volumetric Laser Induced Fluorescence)*, in *32nd AIAA Aerodynamic Measurement Technology and Ground Testing Conference*. 2016, American Institute of Aeronautics and Astronautics.

44. Wu, Y., Lei, Q., Xu, W., and Ma, L., *5 kHz VLIF (Volumetric Laser Induced Fluoresence) Measurements in Turbulent Flows Seeded with Iodine*, in *32nd AIAA Aerodynamic Measurement Technology and Ground Testing Conference*. 2016, American Institute of Aeronautics and Astronautics.

45. Meyer, T.R., Halls, B.R., Jiang, N., Slipchenko, M.N., Roy, S., and Gord, J.R., *High-speed, three-dimensional tomographic laser-induced incandescence imaging of soot volume fraction in turbulent flames.* Optics Express, 2016. **24**(26): p. 29547-29555.

46. Greene, M.L. and Sick, V., *Volume-resolved flame chemiluminescence and laser-induced fluorescence imaging.* Applied Physics B, 2013. **113**(1): p. 87-92.

47. Ma, L., Lei, Q., Capil, T., Hammack, S.D., and Carter, C.D., *Direct comparison of two-dimensional and three-dimensional laser-induced fluorescence measurements on highly turbulent flames.* Optics Letters, 2017. **42**(2): p. 267-270.

48. Ma, L., Lei, Q., Ikeda, J., Xu, W., Wu, Y., and Carter, C.D., *Single-shot 3D flame diagnostic based on volumetric laser induced fluorescence (VLIF).* Proceedings of the Combustion Institute.

49. Halls, B.R., Gord, J.R., Jiang, N., Splichenko, M., Roy, S., and Meyer, T.R., *High-speed three-dimensional tomographic measurements for combustion systems*, in *32nd AIAA Aerodynamic Measurement Technology and Ground Testing Conference*. 2016: Washington, D.C. p. 4027.

50. Kychakoff, G., Paul, P.H., van Cruyningen, I., and Hanson, R.K., *Movies and 3-D images of flowfields using planar laser-induced fluorescence.* Applied Optics, 1987. **26**(13): p. 2498-2500.

51. Nygren, J., Hult, J., Richter, M., Aldén, M., Christensen, M., Hultqvist, A., and Johansson, B., *Three-dimensional laser induced fluorescence of fuel distributions in an HCCI engine.* Proceedings of the Combustion Institute, 2002. **29**(1): p. 679-685.

52. Cho, K.Y., Satija, A., Pourpoint, T.L., Son, S.F., and Lucht, R.P., *High-repetition-rate three-dimensional OH imaging using scanned planar laser-induced fluorescence system for multiphase combustion.* Applied Optics, 2014. **53**(3): p. 316-326.

53. Miller, V.A., Troutman, V.A., and Hanson, R.K., *Near-kHz 3D tracer-based LIF imaging of a co-flow jet using toluene.* Measurement Science and Technology, 2014. **25**(7): p. 075403.

54. Wellander, R., Richter, M., and Aldén, M., *Time-resolved (kHz) 3D imaging of OH PLIF in a flame.* Experiments in Fluids, 2014. **55**(6): p. 1-12.

55. Yip, B., Schmitt, R.L., and Long, M.B., *Instantaneous three-dimensional concentration measurements in turbulent jets and flames.* Optics Letters, 1988. **13**(2): p. 96-98.

56. Yip, B., LAM, J., Winter, M., and LONG, M., *Time-resolved three-dimensional concentration measurements in a gas jet.* Science, 1987. **235**(4793): p. 1209-1211.

57. Wilkes, J., Glass, C., Danehy, P., and Nowak, R. *Fluorescence imaging of underexpanded jets and comparison with CFD*. in *44th AIAA Aerospace Sciences Meeting and Exhibit*. 2006.

58. Danehy, P., Bathel, B., Ivey, C., Inman, J., and Jones, S. *NO PLIF study of hypersonic transition over a discrete hemispherical roughness element*. in *47th AIAA Aerospace Sciences Meeting including The New Horizons Forum and Aerospace Exposition*. 2009.

59. Eckbreth, A.C., *Laser diagnostics for combustion temperature and species, chapter 9*. Vol. 3. 1996: CRC Press.

Chapter 2 3D flame topography obtained by tomographic chemiluminescence with direct comparison to planar Mie scattering measurement

(Published on Applied Optics, 54 (2015) 2174-2182)
Wenjiang Xu, A.J. Wickersham, Yue Wu, Fan He, Lin Ma

Abstract

This work reports the measurements of 3D (three-dimensional) flame topography using tomographic chemiluminescence, and its validation by a direct comparison against planar Mie scattering measurements. Tomographic measurements of the 3D topography of various well-controlled laboratory flames were performed using projections measured by seven cameras, and a simultaneous Mie scattering measurement was performed to measure a 2D cross-section of the 3D flame topography. The tomographic measurements were based on chemiluminescence emissions from the flame, and the Mie scattering measurements based on micron-size oil droplets seeded into the flow. The flame topography derived from the 3D tomographic and the Mie scattering measurement were then directly compared. The results show that the flame topography obtained from tomographic chemiluminescence and the Mie measurement agreed qualitatively (i.e., both methods yielded the same profile of the flame fronts), but quantitative difference on the order of millimeter was observed between these two methods. These results are expected to be useful both for understanding the capabilities and limitations of both the 3D tomographic technique and the Mie scattering technique in combustion diagnostics.

Introduction

Turbulent premixed flames represent both a significant and scientific problem with many practical applications. Scientifically, many open questions still exist in our understanding of the governing processes of such flames, and a better understanding of these processes forms the cornerstone to construct and improve a wide range of practical power and propulsion devices [1]. The characteristics of flame fronts hold a pivotal position in the study of premixed turbulent flames, and some of the key characteristics include the location and curvature of the flame front, flame surface density, and flame brush thickness. As a result, extensive research efforts have been invested to experimentally measure these characteristics in various premixed turbulent flames [2-7]. These past efforts can be broadly divided into three categories based on how the flame front is defined and corresponding experimental technique used. In the first category, the flame front is imaged via planar laser induced fluorescence (PLIF) based on a flame radical such as OH or CH [2, 6]. These intermediate flame radicals serve as a marker for the boundary between burnt and unburnt gases, and therefore images of their distribution (obtained via PLIF) can be used to infer structure of the flame fronts. In the second category, the flame front is imaged via planar Mie scattering from small droplets (typically micron-sized oil droplets) seeded in the air/fuel mixture [4, 5]. Under well-designed conditions, the seeded droplets evaporate immediately before they enter the flame front. Therefore, the distribution of the seeded droplets (imaged via Mie scattering) can also be used to infer the boundary between burnt and unburnt gases and thus the structure of the flame front. In the third category, the flame front is imaged via chemiluminescence emissions from flame radicals such as CH* and OH* [8-10]. Similar

to the CH and OH radicals used in the PLIF approach, these chemiluminescence species can also serve as a marker for the flame front and measurements of their distribution can be used to infer characteristics of the flame front.

All three categories of techniques have been extensively studied and applied in the past, and their capabilities and limitations relatively well understood. A limitation common to all three approaches is that they only provide 1D or 2D measurements, while the flame front structure is inherently 3D for turbulent flames. Active research efforts are currently ongoing to investigate the extension to 3D measurements of all three approaches. This work focuses on techniques in the second and third category, more specifically, on the extension of the chemiluminescence technique for 3D measurements with direction comparison against Mie scattering measurements.

With the advancement of camera and computational technologies, recent work has demonstrated the feasibility of combining chemiluminescence with tomography, referred to as tomographic chemiluminescence (TC) here, to obtain instantaneous 3D flame measurements [7, 11-15]. The TC technique employs multiple cameras to obtain 2D projection measurements of the target flame from different perspectives. Using the measured projections as inputs, a tomographic inversion is then performed to obtain the 3D flame structure. Past efforts have demonstrated the ability of the technique to obtain instantaneous 3D flame measurements with temporal resolution above multi-kHz (20 kHz measurements have been demonstrated recently with intensified cameras [16]), spatial resolution below millimeter, in a volume with dimension on the order of decimeter. These past results illustrate the advantages and capabilities of the TC technique and motivate further research [14]. One of the key research needs for the further development

of the TC technique involves the validation of the 3D measurements (a research need shared also by other tomographic-based 3D diagnostics). Several methods have been developed and applied in these past research efforts for validation purposes, including numerical simulations based on phantoms [7, 12, 15, 17], use of controlled flames with known patterns [11, 15, 18], and comparison between 3D results obtained experimentally and simulated results obtained via ray-tracing [19, 20]. Further validation is always desired for the development of new diagnostic tools, and the validation method should ideally be as direct as possible.

Therefore, this work describes an additional validation method by a direct comparison between the 3D TC measurements and 2D Mie scattering measurements. Note that the Mie scattering method itself can be extended to 3D measurements as well either by combining with tomography also [16, 21, 22] or by a rapid scanning of the illumination laser sheet [23]. However, the goal of this work is to use the Mie scattering technique to provide a validation for the 3D TC technique, and therefore the Mie scattering technique was applied in its well-established planar fashion. Specifically, measurements of flame topography were performed on several target flames by the TC and planar Mie scattering techniques simultaneously. The TC measurements provided 3D topography and the Mie scattering measurements provided a 2D cross-section of the 3D topography across the plane illuminated by the laser sheet. The 2D cross-sectional Mie measurements were then directly compared to the 3D measurements at the illuminated plane for validation purposes. Such comparison is also expected to be useful beyond the validation of 3D measurements, because both chemiluminescence and Mie scattering techniques are extensively applied for flame visualization. Some comparative results reported in this

work should elucidate several aspects of the general use of chemiluminescence and Mie scattering techniques. Due to the validation nature of this work, the experiments were performed on relatively simple flames, however both the chemiluminescence and Mie scattering techniques can be applied to more complicated turbulent flames, and both their applications and limitations have been discussed in more details elsewhere [4, 5].

Experimental Setup

The schematic of the experimental arrangement used in this work is shown in Fig. 2-1. A total of eight cameras were used in the setup as shown: seven CMOS cameras (Photron SA4s and SA6s) for the TC measurements and one CCD camera (Andor SensiCam) for the Mie scattering measurements. The Mie measurements were based on the scattering from micron-sized droplets of olive oil (with mean diameter around 2 μm) seeded in the fuel/air mixture. The oil droplets were illuminated by a thin laser sheet with a thickness of ~3 mm generated from a 10 Hz Nd:YAG pulse laser (at a wavelength of 532 nm and with a pulse width of ~ 8 ns). Due to limitation of the 10 Hz repetition rate of the laser, both the Mie scattering and TC measurements were performed at 10 Hz in this work. More specifically, both the CCD and CMOS cameras were synchronized with the laser at a frame rate of 10 Hz. An exposure time of 1 ms was used for all cameras. The measurement duration of the Mie scattering measurements was defined by the pulse width of the illumination laser (~ 8 ns), not by the exposure time of the CCD camera. The measurement duration for the TC measurements was defined by the exposure time of the CMOS cameras, and 1 ms was short enough to freeze the motion of the flames used in this work. The flames used in this work were tested to be stable (within our detection ion limit) for at least a few seconds, a time frame much longer than the actual measurement

duration. Before taking any measurement, several seconds worth (i.e., a few thousands) of pictures were taken by each camera for the target flame, and no observable variation of the flame were found in any two sequential pictures. A shorter exposure time should be used for more dynamic and turbulent flames. Sufficient signals were observed for both the TC and Mie scattering measurements, and measurements at higher repetition rates and lower exposure times should be feasible if an illumination laser with a higher repetition rate was available when this work was performed. Nonetheless, the repetition rate of the measurement is not essential for the purpose of cross-comparison and validation.

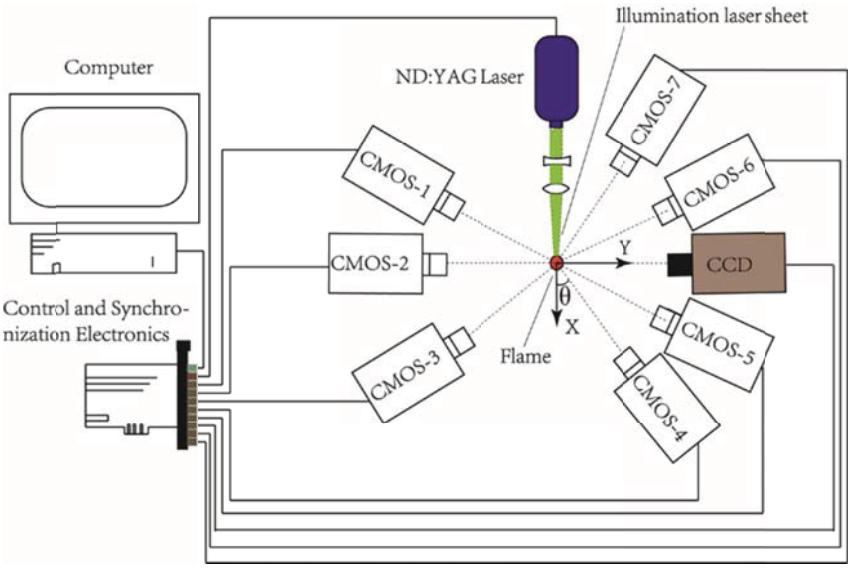

Fig. 2-1. Schematic of the experimental setup.

Measurements were performed on several target flames generated by different burners and using methane and propane (CH_4 and C_3H_8) as fuel. The flames were all operated under atmospheric pressure and room temperature. The volumetric flow rates of fuel and oxidizer was 0.8 and 5.7 standard liter per minute (SLPM) for CH_4/air flame, 0.5 and 0.98 SLPM for C_3H_8/O_2 flame, and 0.5 and 3.3 SLPM for C_3H_8/air flame,

respectively. These flames were designed to compare the TC and Mie scattering measurements under several different representative conditions. Based on the configuration of the laser sheet and burner, the following Cartesian coordinate system was established to facilitate the discussion: the origin was defined at the center of the burner, the *X* axis was defined along the direction of the illuminating laser sheet (which was aligned to pass through the center of the burner), and the *Z* axis was defined to be along the direction of the flow.

The oil droplets were generated by an aerosol generator using a Laskin nozzle (TSI Droplet Generator 9307). The requirements for the oil droplets to serve as marker of the flame front have been well understood from past efforts [3-5, 24]. These requirements include: 1) the seeded droplets need to be small enough to faithfully follow the velocity fluctuations and evaporate in a short time compared to the time it takes for them to pass through the flame front, and 2) the seeded droplets must not significantly alter the flame physics or chemistry. The first requirement is typically met with droplet diameter smaller than ~ 5 μm, and the second one met with seeding a small amount of oil relative to the fuel/air mixture, typically on the order of 0.01% by mass fraction [4]. Both requirements were met in this work by choosing the proper combination of operation conditions for the aerosol generator and the burners.

Prior to any flame measurement, the location and orientation of all the cameras were calibrated using a view registration procedure as detailed in [18, 25]. A calibration target with known chessboard pattern was placed on top of the burner and one of its calibrating surfaces aligned in the same plane as the illuminating laser sheet. Images of the calibration target were then captured by all the cameras, and the chessboard pattern

was magnified and distorted to different degrees on each camera. Such differences depend on the relative orientation and location of the cameras to the calibration target, and were analyzed using a view registration program to determine the orientation and location of each camera. The orientations of the cameras determined by the view registration procedure were 90° for the CCD camera, and 220.22°, 269.25°, 304.16°, 34.68°, 64.99°, 113.26°, and 146.91° for the CMOS cameras 1 through 7, respectively. Note that the second CMOS camera and the CCD camera were intentionally aligned to be opposite of each other to facilitate the comparison of the measurements for these two cameras.

2D comparison and analysis

This section first analyzes the results in 2D by comparing the planar Mie images against the line-of-sight integrated chemiluminescence measurements taken from an opposite direction. The goal of the analysis reported in this section is to establish a baseline of the differences between the Mie and chemiluminescence techniques to prepare for the analysis in 3D.

Fig. 2-2A and Fig. 2-2B show a set of flame images captured by the Mie scattering technique on the CCD camera and the chemiluminescence technique on CMOS camera 2, respectively. The pixel resolution for the results shown here is 400×400, with each pixel corresponding to a physical dimension of 20 microns. Note that images shown in Fig. 2-2A and Fig. 2-2B are mirror images of each other due to the way these cameras were aligned as shown in Fig. 2-1. The flame in this case was a premixed CH_4/air flame generated by a circular jet with a diameter of 12 mm. The flame has an approximate cone shape with an overall height of about 25mm as shown. The bright region seen in Fig.

2-2A is due to the Mie scattering from the seed oil droplets and represents the unburnt regime as aforementioned. The dark region in Fig. 2-2A is due to the lack of Mie scattering because of the absence of oil droplets due to evaporation near the flame front. An edge detection algorithm based on the sharpest gradient in the image was implemented to find the boundary between the bright and dark region, resulting in the flame front (the orange curve) shown in Fig. 2-2C overlapped on the Mie scattering image itself. For the chemiluminescence image shown in Fig. 2-2B, an outer and an inner boundary were found using the same edge detection algorithm, and the inner boundary were used in this work to define the flame front, as shown in Fig. 2-2D (again overlapped on the chemiluminescence image itself).

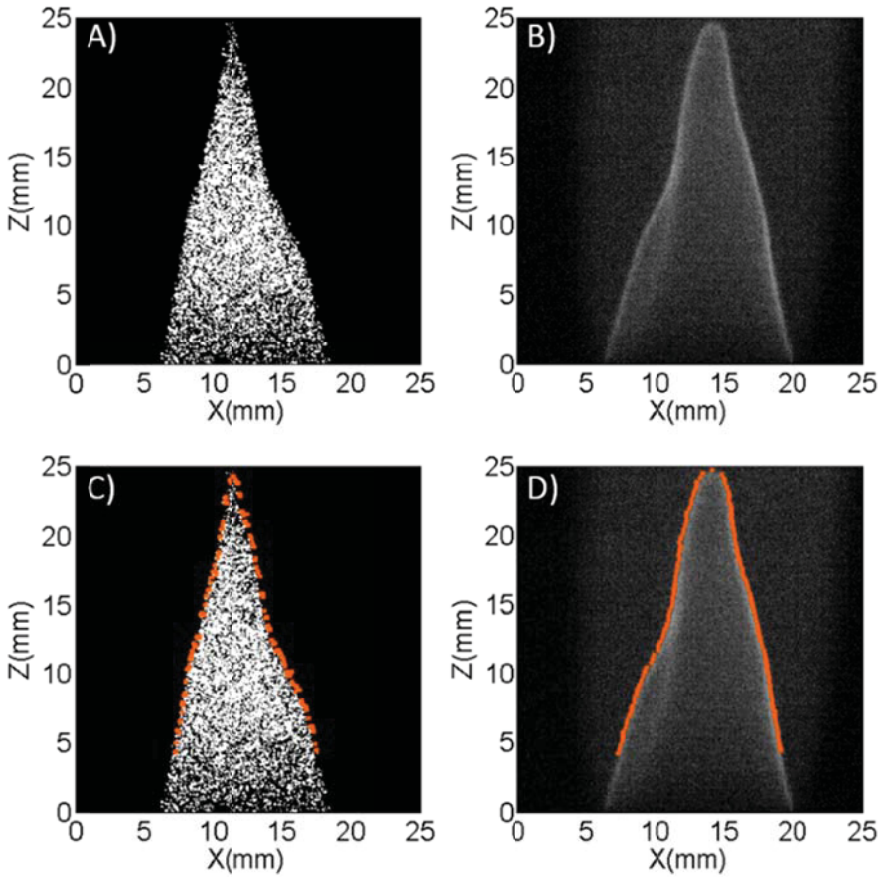

Fig. 2-2. A) Mie scattering image of a premixed CH_4 flame. B) Simultaneous chemiluminescence measurement. C) Flame front derived from the Mie scattering image.

D) Flame front derived from the chemiluminescence image.

Based on the flame fronts shown in Fig. 2-2C and Fig. 2-2D, the location of the flame front can be digitized as shown in Fig. 2-3A. Fig. 2-3A clearly illustrates the similarities and differences of the flame fronts measured (or defined) by the Mie and chemiluminescence techniques. Both techniques captured the same profile of the cone-shaped flame qualitatively, but not quantitatively. To quantify the discrepancy, Fig. 2-3B shows the differences of the location of the flame front along the local norm on the flame front (denoted as Δ) measured by both techniques.The discrepancy seen here is both due to the fundamental differences in how the flame front is defined and also practical implementation issues. The flame front is defined by the temperature profile in the pre-heat zone in the Mie scattering technique, and by the intensity of chemical reactions in the chemiluminescence technique in contrast **[4, 26]**. As a result, the flame front measured by the chemiluminescence technique (even when the inner edge was used here) was observed to be further away from the reactants compared to that measured by the Mie scattering technique as seen in Fig. 2-3A. The difference was within a range of 0.8 to 1.6 mm for this particular flame, with an arithmetic average of 1.25 mm.

Similar to Fig. 2-2 and Fig. 2-3, Fig. 2-4 and Fig. 2-5 compare the Mie scattering and chemiluminescence measurements for a C_3H_8/O_2 flame. The flame was generated with the same burner used in Fig. 2-2 and Fig. 2-3. However, due to the Lewis number effects **[26]**, the C_3H_8/O_2 flame features an open tip in contrast to the closed tip seen in the CH_4/air flame discussed above. Fig. 2-4A and Fig. 2-4B show the Mie scattering and chemiluminescence images, and Fig. 2-4C and Fig. 2-4D show the corresponding flame fronts derived from these images. As mentioned earlier, these flames were designed to examine the accuracy of the Mie and TC techniques under different representative

conditions. For instance, these results illustrate a limitation of the Mie scattering technique in flames with an open tip. The measurement shown in Fig. 2-4A by itself was insufficient to differentiate this open-tip flame from the close-tip CH_4/air flame shown in Fig. 2-2. Fig. 2-5A and Fig. 2-5B show the digitized flame fronts obtained and Δ. For this flame, Δ was in the range of 0.8 to 1.8 mm with an arithmetic average of 1.2 mm.

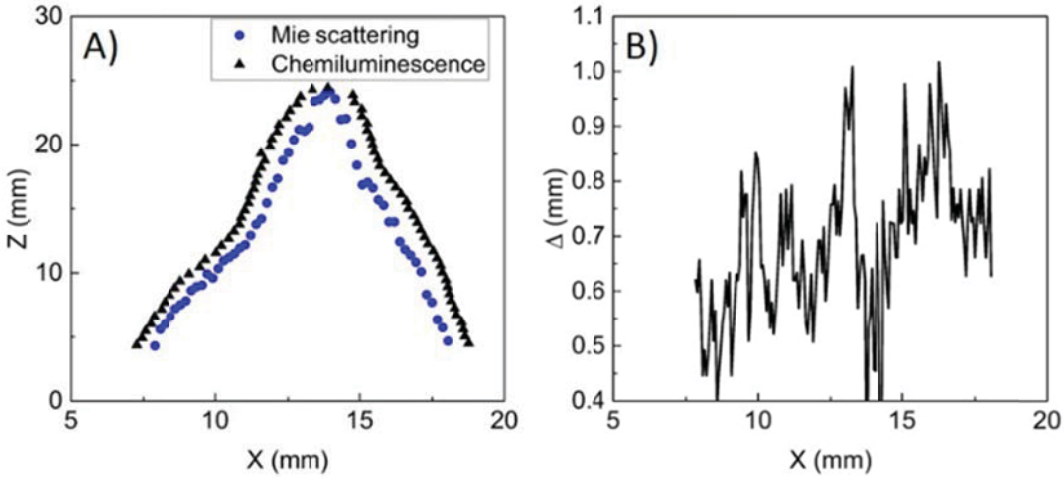

Fig. 2-3. A) Flame front obtained from the Mie scattering and chemiluminescence measurements. B) The differences between the Mie scattering and chemiluminescence measurements.

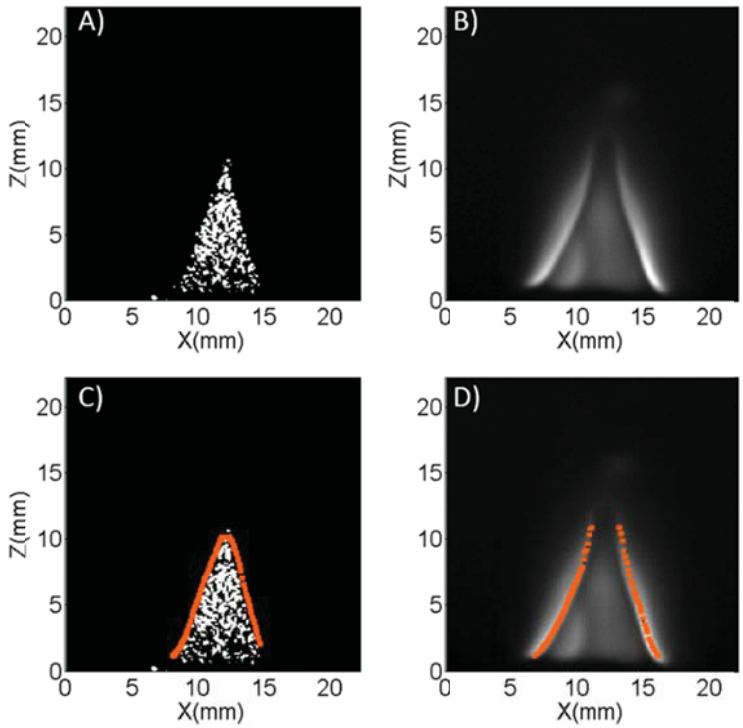

Fig. 2-4. A) Mie scattering image of a premixed CH_4 flame. B) Simultaneous chemiluminescence measurement. C) Flame front derived from the Mie scattering image. D) Flame front derived from the chemiluminescence image.

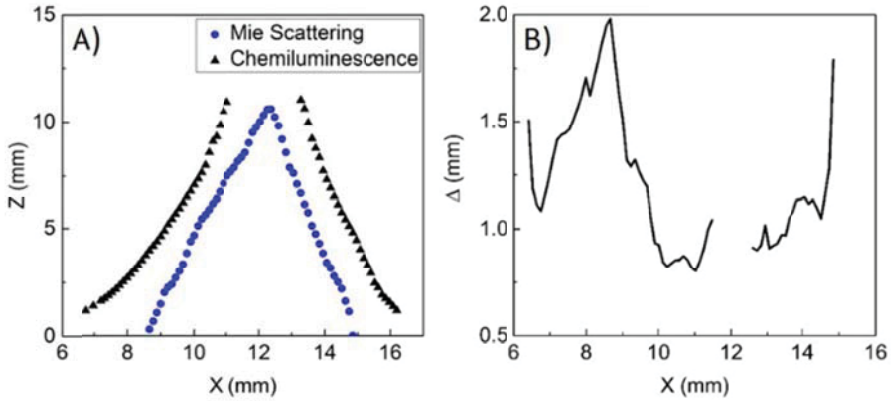

Fig. 2-5. A) Flame front obtained from the Mie scattering and chemiluminescence measurements. B) The differences between the Mie scattering and chemiluminescence measurements.

3D reconstruction and Mie scattering comparison

Based on the 2D analyses described in Section 3, this section reports the comparison between the 3D TC results and the Mie scattering results. The 3D reconstruction was performed using a variation of the ART (Algebraic Reconstruction Technique) inversion algorithm that was tested and applied in several other tomographic combustion measurements [15, 27, 28]. The reconstruction process is briefly summarized here using the sample results shown in Fig. 2-6.

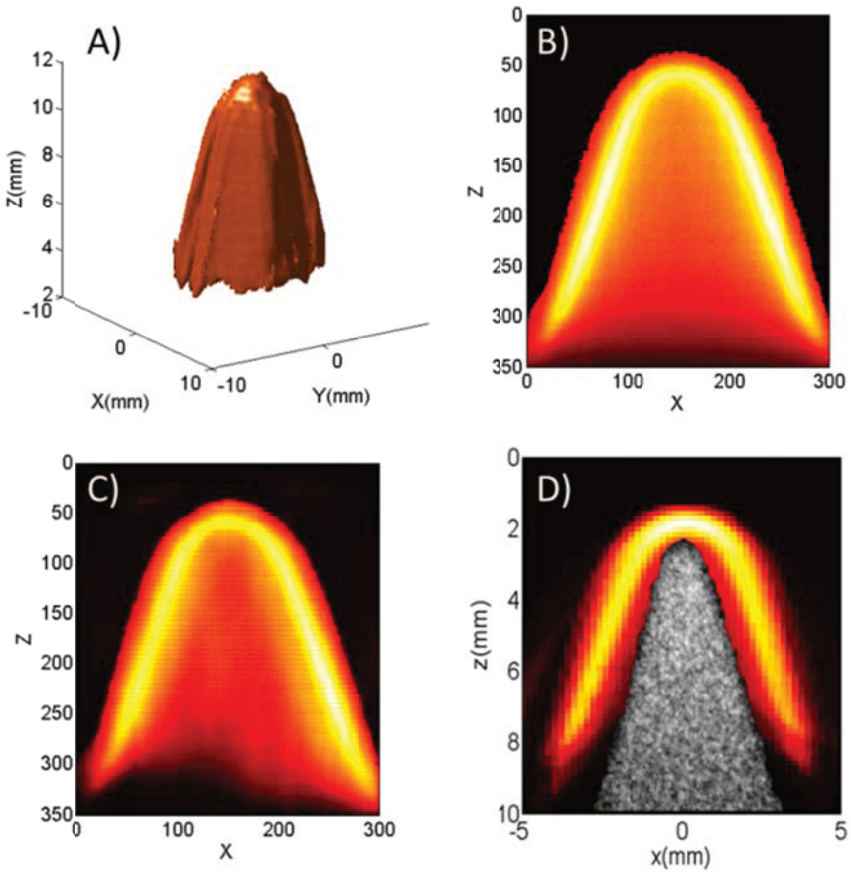

Fig. 2-6. A) A 3D rendering of the topography of the premixed CH_4 cone shape flame measured by the 3D TC technique. B) Projection measured by CMOS camera 2. C) Projection simulated via ray-tracing. The simulation was made along the same orientation as camera 2. D) Overlapping of the Mie scattering and TC slice along the same orientation as camera 2.

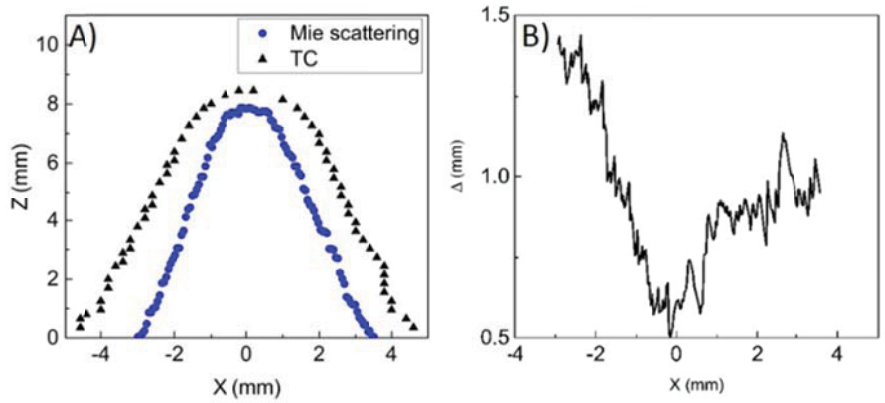

Fig. 2-7. A) Flame front obtained from the Mie scattering and TC techniques. B) The differences between the Mie scattering and TC techniques.

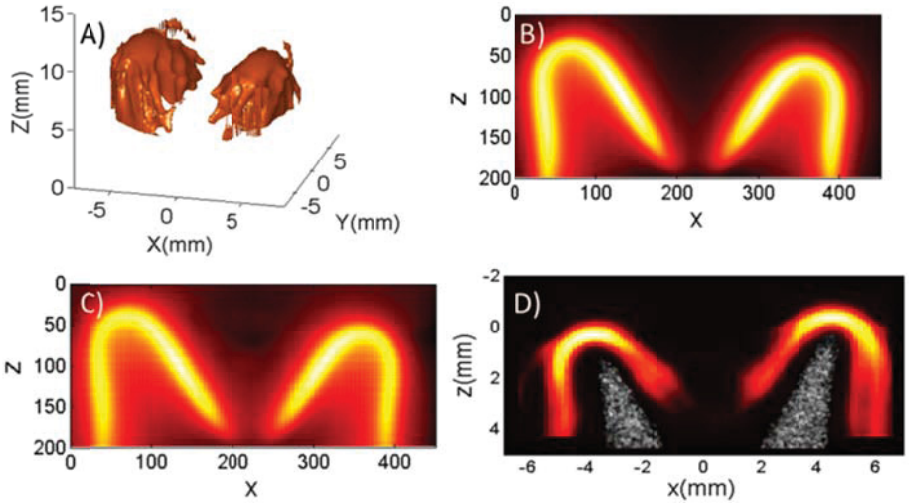

Fig. 2-8. A) A 3D rendering of the topography of the premixed CH_4 V-shaped flame measured by the 3D TC technique. B) Projection measured by CMOS camera 2. C) Projection simulated via ray-tracing. The simulation was made along the same orientation as camera 2. D) Overlapping of the Mie scattering and TC slice along the same orientation as camera 2.

Fig. 2-6A shows a 3D rendering of the topography of a premixed jet CH_4./air flame measured by the TC technique. The tomographic reconstruction was performed using the projection measurements of chemiluminescence captured by the seven CMOS cameras, with one such example projection captured by camera 2 shown in Fig. 2-6B. This particular flame was approximately axially symmetric, however no *a priori*

knowledge about the symmetry (or the lack of symmetry) was assumed in the tomographic reconstruction in this work (neither in this particular measurement nor in the other measurements discussed). The tomographic reconstruction consisted of three steps. In the first step, the measured projections were cropped to reduce computational cost and memory requirements. Dark regions with no signal corresponded to regions with no flame, and these regions were cropped from the raw chemiluminescence images. For instance, the projection measurement shown in Fig. 2-6B is an image after cropping, and this cropped image had a pixel resolution of 350×300. In the second step, a measurement volume was defined to encompass the entire flame, and the measurement volume was discretized into Cartesian voxels. For instance, a measurement volume of 20×20×20 mm was defined for the flame shown here, and this volume was discretized into 64×64×64 voxels (approximately 2.6×10^5 voxels), resulting in a nominal spatial resolution of 0.32 mm in all three directions.

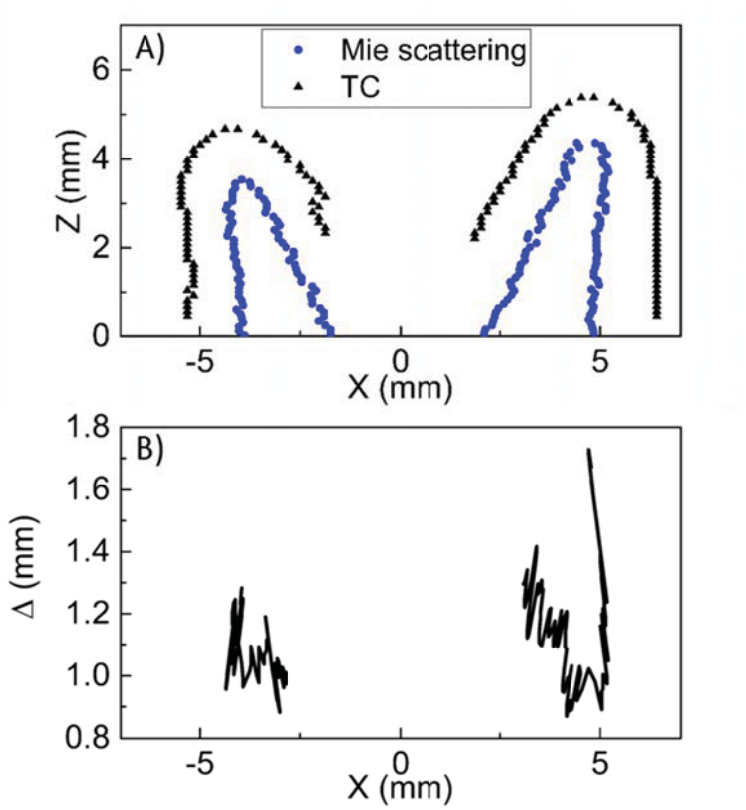

Fig. 2-9. A) Flame front obtained from the Mie scattering and TC techniques. B) The differences between the Mie scattering and TC techniques.

Fig. 2-6C shows the projection simulated via a ray-tracing program as described in [19, 29] based on the 3D reconstruction shown in Fig. 2-6A. The simulation was made along the same orientation as camera 2. As can be seen, the close agreement between the measured projection shown in Fig. 2-6B and the simulated projection shown in Fig. 2-6C supports the correctness of the tomographic inversion but does not prove it conclusively.

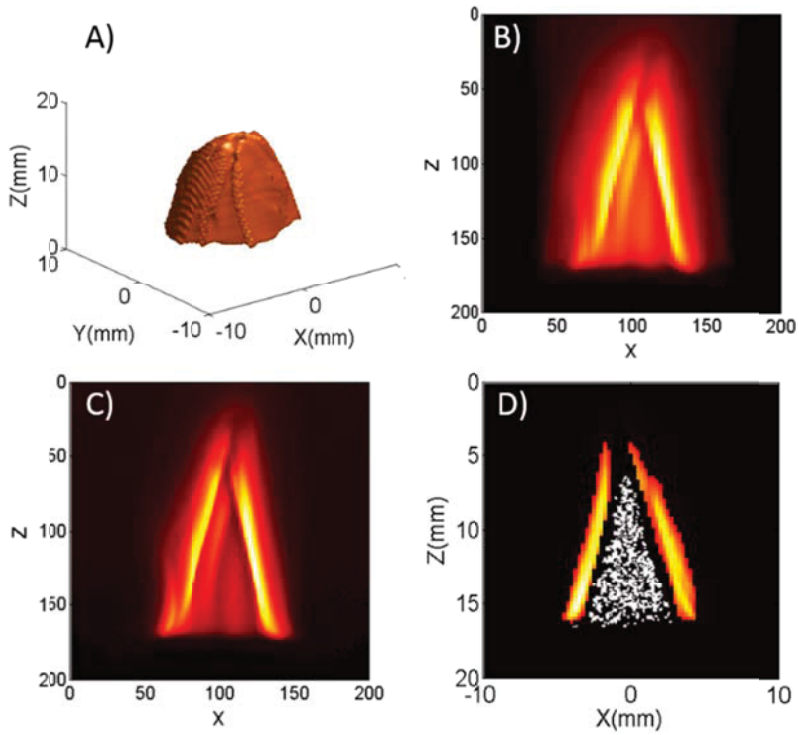

Fig. 2-10. A) A 3D rendering of the topography of the premixed C_3H_8 cone shape flame measured by the 3D TC technique. B) Projection measured by CMOS camera 2. C) Projection simulated via ray-tracing. The simulation was made along the same orientation as camera 2. D) Overlapping of the Mie scattering and TC slice along the same orientation as camera 2.

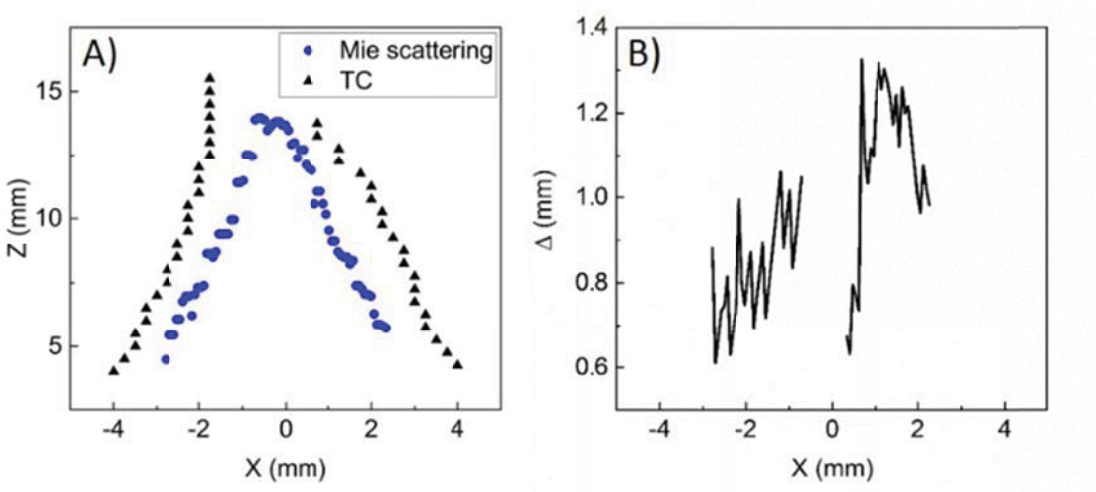

Fig. 2-11. A) Flame front obtained from the Mie scattering and TC techniques. B) The differences between the Mie scattering and TC techniques

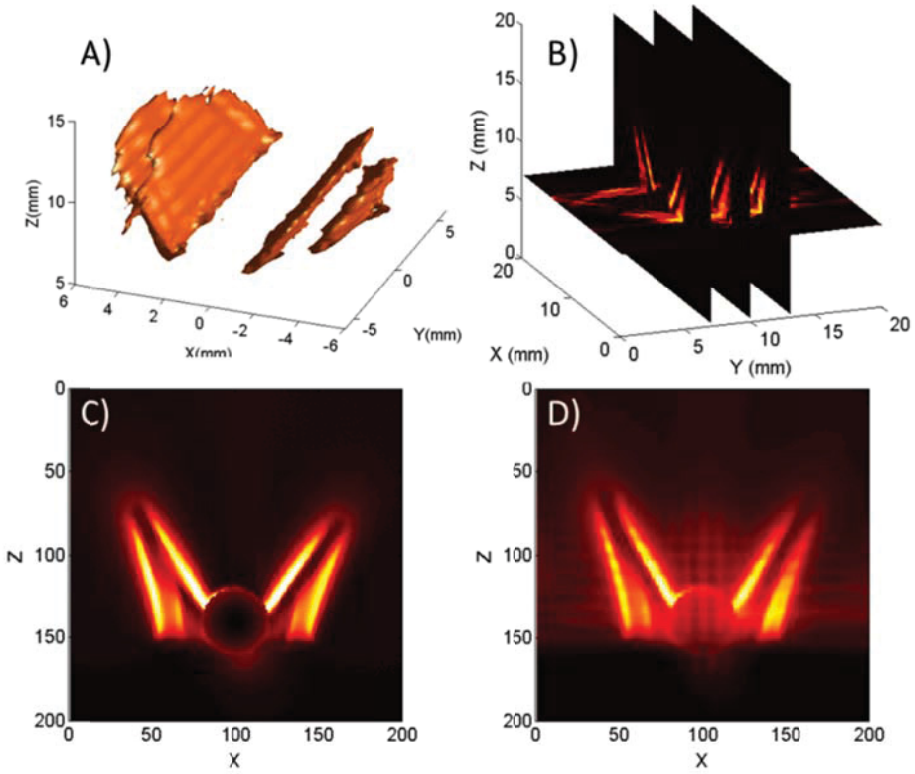

Fig. 2-12. A) A 3D rendering of the topography of the premixed C_3H_8 V-shaped flame measured by the 3D TC technique (also see Media). B) Three cross-sectional views of the 3D measurement along the central plane. C) Projection measured by CMOS camera 2. D) Projection simulated via ray-tracing. The simulation was made along the same orientation as camera 2.

As motivated earlier, a key goal of this work is to provide direct validation of the 3D reconstruction via Mie scattering measurements, as shown in Fig. 2-6D. In Fig. 2-6D, the Mie scattering image is overlapped with the cross-sectional view of the 3D topography shown in Fig. 2-6A across the plane of the illumination laser sheet (i.e., the plane at y=0 mm). Based on the results shown in Fig. 2-6D, edge detection was performed using the same method as discussed in Section 3 to obtain the position of the flame fronts. Fig. 2-7A shows the position of the flame fronts obtained, and Fig. 2-7B shows the difference between the flame fronts measured by the Mie and TC techniques. The discrepancy seen in Fig. 2-7B was caused by several factors: 1) the difference in the

definitions of the flame front on which the Mie and TC techniques are based as discussed in Section 3, 2) the uncertainty in the 3D TC measurements, and 3) experimental uncertainties associated with both the Mie and TC measurements. It is difficult to isolate these factors experimentally. However, the discrepancy seen on Fig. 2-7B is in the same range as that seen on Fig. 2-3B, providing a direct validation of the 3D measurements within the experimental uncertainty of established 2D measurements.

Fig. 2-8 to Fig. 2-13 show another three sets of similar results obtained on three different flames. More specifically, Fig. 2-8 and Fig. 2-9 show the results obtained on another closed-tip CH_4 flame. Compared to the simple cone-shaped flame used in Fig. 2-6 and Fig. 2-7, this flame had a more complicated V-shape created by placing a tungsten rod at the exit of the jet. Fig. 2-8A shows a 3D rendering of the topography of the V-shaped flame measured by the TC technique. The projection measurement taken by camera 2 is shown in Fig. 2-8B, which was in agreement with the simulated projection shown in Fig. 2-8C (again simulated by the ray-tracing program based on the 3D reconstruction shown in Fig. 2-8A). Fig. 2-8D shows the comparison between the 3D tomographic reconstruction and the Mie measurements across the central plane of the flame (i.e., the plane with y=0 mm). Similar to the cone flame studied above, edge detection was performed on Fig. 2-8D to extract the flame front positions. Fig. 2-9A shows such positions of the flame fronts, and Fig. 2-9B shows the difference between such two fronts. Because of the V-shape of the flame, the differences in Fig. 2-9B appear in two branches. The arithmetic average for the difference shown here is 0.84 mm.

Fig. 2-10 and Fig. 2-11 show the results obtained on an open-tip C_3H_8/air flame. Fig. 2-10A shows a 3D rendering of the topography of the open tip C_3H_8/air cone flame

measured by the TC technique. Note that the open-tip is not apparent in Fig. 2-10A only due to the visual limitation of the software we used for 3D rendering. The open-tip feature was captured accurately by the 3D reconstruction, as seen clearly from the cross-sectional view of the 3D reconstruction shown in Fig. 2-10D. Fig. 2-10B and Fig. 2-10C again compare the measured and simulated projections, and Fig. 2-10D the TC and Mie measurements at the central plane. Fig. 2-11 compares the edges of the flame detected by the TC and Mie techniques. The arithmetic average of the difference shown in Fig. 2-11B is 1.2 mm.

Lastly, Fig. 2-12 and Fig. 2-13 show the results obtained on an open-tip C_3H_8/air jet flame with a tungsten rod placed at the jet exit. In this case, the flame consisted of four separate sections, due to the open-tip feature and the V-shaped arrangement. Fig. 2-12A shows the 3D reconstruction, Fig. 2-12B shows the cross-sectional views of the reconstruction from several perspectives for better visualization, and Fig. 2-12C and Fig. 2-12D compares the measured and simulated projections, respectively. Fig. 2-13A compares the TC and Mie measurements across the central plane, Fig. 2-13B compares the flame edges extracted, and Fig. 2-13C the differences in the flame edges. The arithmetic average of the difference shown here is 1.2 mm. A detailed illustration of the 3D reconstruction of this flame in Fig. 2-12A (Media) is included in the accompanying video by showing its 360^0 rotation view.

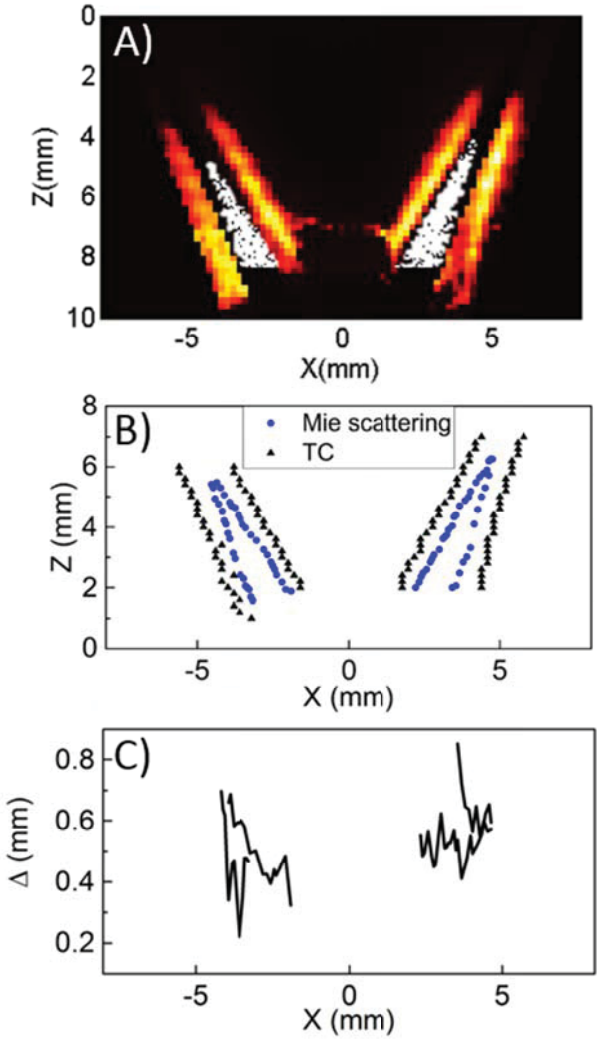

Fig. 2-13. A) Overlapping of the Mie scattering and TC slice along the same orientation as camera 2. B) Flame front obtained from the Mie scattering and TC techniques. C) The differences between the Mie scattering and TC techniques

Several observations can be made from these results. First, the 3D flame edges extracted from the TC technique showed consistent agreement with those obtained from the planar Mie technique. The agreement was consistently about 1 mm, which was within the same range as the 2D analysis discussed in Section 3. Second, these results also illustrate the limitations of both the TC and Mie techniques. Each technique is based on a fundamentally different definition of the flame front. The Mie technique encounters limitations when applied to flames with complicated features, for example, its ability to

differentiate open-tip flames from closed-tip flames. Lastly, these comparisons also illustrate the limitation of 2D diagnostics and motivate the needs for 3D diagnostics to resolve complicated flows and flames. For example, the Mie scattering technique measures a planar cross-section of the 3D flame topography, and is therefore dependent on the orientation of the measurement. In this work, the particular orientation has been chosen to be one that can provide the most well defined quantities (e.g., thickness of the flame) and has been assumed to be known a priori, which is not usually the case in practice.

Summary and conclusion

In summary, this work focused on the measurements of 3D flame topography using two techniques: tomographic chemiluminescence (TC) and planar Mie scattering. The 3D flame front measured by the TC technique was directly compared against that measured by the planar Mie scattering technique. The TC measurements were implemented with a total of 7 CMOS cameras, providing projections from 7 views as inputs to the subsequent 3D tomographic reconstruction. The planar Mie scattering measurements were implemented simultaneously with a CCD camera based on micron oil droplets seeded in the flow.

The measurements were first analyzed in 2D for a simple cone flame to establish a baseline of their differences. The results show that the flame topography obtained from chemiluminescence and Mie measurements agreed qualitatively (in terms of the overall profile of the flame edges), but not quantitatively. For the flames used in this work, a difference on the order of 1 mm was observed between these two methods. Then, 3D

measurements obtained from the TC technique were compared to the planar Mie technique. Various control flames were designed to compare these two techniques, including simple cone flames with a single flame front and flames with multiple branches and fronts. Comparison under all cases show a consistent agreement between the flame edges extracted from the 3D TC technique and the planar Mie technique. The agreement was consistently about 1 mm, which was within the baseline established by the 2D analysis. These results are expected to be useful for both validating the 3D TC technique, and also for understanding the capabilities and limitations of chemiluminescence and Mie scattering as combustion diagnostics.

Acknowledgment

The authors gratefully acknowledge the support from the National Science Foundation (Award CBET 1156564). Wenjiang Xu was supported by a Dean's Incentive Fund provided by Virginia Tech during this work.

References

1. Driscoll, J.F., *Turbulent premixed combustion: Flamelet structure and its effect on turbulent burning velocities.* Progress in Energy and Combustion Science, 2008. **34**(1): p. 91-134.

2. Filatyev, S.A., Driscoll, J.F., Carter, C.D., and Donbar, J.M., *Measured properties of turbulent premixed flames for model assessment, including burning velocities, stretch rates, and surface densities.* Combustion and Flame, 2005. **141**(1-2): p. 1-21.

3. Kheirkhah, S. and Guelder, O.L., *Turbulent premixed combustion in V-shaped flames: Characteristics of flame front.* Physics of Fluids, 2013. **25**(5).

4. Miles, P.C. and Gouldin, F.C., *Premixed turbulent flame/flow interaction: Simultaneous measurements of velocity and flamelet position.* Aiaa Journal, 1998. **36**(7): p. 1178-1189.

5. Shepherd, I.G., *Flame surface density and burning rate in premixed turbulent flames*. Twenty-Sixth Symposium, ed. A.R. Burgess and F.L. Dryer. 1996. 373-379.

6. Hult, J., Gashi, S., Chakraborty, N., Klein, M., Jenkins, K.W., Cant, S., and Kaminski, C.F., *Measurement of flame surface density for turbulent premixed flames using PLIF and DNS.* Proceedings of the Combustion Institute, 2007. **31**: p. 1319-1326.

7. Floyd, J., Geipel, P., and Kempf, A.M., *Computed Tomography of Chemiluminescence (CTC): Instantaneous 3D measurements and Phantom studies of a turbulent opposed jet flame.* Combust. Flame, 2011. **158**(2): p. 376-391.

8. Kojima, J., Ikeda, Y., and Nakajima, T., *Spatially resolved measurement of OH*, CH*, and C_2* chemiluminescence in the reaction zone of laminar methane/air premixed flames.* Proc. Combust. Inst., 2000. **28**: p. 1757-1764.

9. Kojima, J., Ikeda, Y., and Nakajima, T., *Basic aspects of OH(A), CH(A), and C_2(d) chemiluminescence in the reaction zone of laminar methane-air premixed flames.* Combust. Flame, 2005. **140**(1-2): p. 34-45.

10. Hardalupas, Y., Panoutsos, C.S., and Taylor, A.M.K.P., *Spatial resolution of a chemiluminescence sensor for local heat-release rate and equivalence ratio*

measurements in a model gas turbine combustor. Exp. Fluids, 2010. **49**(4): p. 883-909.

11. Floyd, J. and Kempf, A.M., *Computed Tomography of Chemiluminescence (CTC): High resolution and instantaneous 3-D measurements of a Matrix burner.* Proc. Combust. Inst., 2011. **33**: p. 751-758.

12. Denisova, N., Tretyakov, P., and Tupikin, A., *Emission tomography in flame diagnostics.* Combustion and Flame, 2013. **160**(3): p. 577-588.

13. Li, X. and Ma, L., *Volumetric imaging of turbulent reactive flows at kHz based on computed tomography.* Optics Express, 2014. **22**(4): p. 4768-4778.

14. Li, X. and Ma, L., *Capabilities and limitations of 3D flame measurements based on computed tomography of chemiluminescence.* Combustion and Flame, 2014. **in press**.

15. Cai, W., Li, X., Li, F., and Ma, L., *Numerical and experimental validation of a three-dimensional combustion diagnostic based on tomographic chemiluminescence.* Optics Express, 2013. **21**(6): p. 7050-7064.

16. Wu, Y., Lei, Q., and Ma, L., *Experimental demonstration of 4D imaging in two-phase flows based on computed tomography at 5 kHz.* APPLIED OPTICS, 2014. **53**(24): p. 5547-5553.

17. Cai, W., Li, X., and Ma, L., *Practical aspects of implementing three-dimensional tomography inversion for volumetric flame imaging.* Applied Optics, 2013. **52**(33): p. 8106-8116.

18. MinWook Kang, Y.W., Lin Ma, *Fiber-Based Endoscopes for 3D Combustion Measurements:View Registration and Spatial Resolution.* Combustion and Flame, 2014. **16**(12): p. 3063–3072.

19. Zhao, Y., Li, X., and Ma, L., *Multidimensional Monte Carlo model for two-photon laser-induced fluorescence and amplified spontaneous emission.* COMPUTER PHYSICS COMMUNICATIONS, 2012. **183**(8): p. 1588-1595.

20. Li, X. and Ma, L., *Three-Dimensional Measurements of Turbulent Jet Flames at kHz Rate Based on Tomographic Chemiluminescence* in *AIAA SciTech 2014, Paper AIAA-2014-0735*. 2014: National Harbor, MD.

21. Lei, Q., Wu, Y., Xiao, H., and Ma, L., *Analysis of four-dimensional Mie imaging using fiber-based endoscopes.* Applied Optics, 2014. **53**(28): p. 6389-6398.

22. Upton, T.D., Verhoeven, D.D., and Hudgins, D.E., *High-resolution computed tomography of a turbulent reacting flow.* Experiments in Fluids, 2011. **50**(1): p. 125-134.

23. Wellander, R., Richter, M., and Alden, M., *Time resolved, 3D imaging (4D) of two phase flow at a repetition rate of 1 kHz.* Optics Express, 2011. **19**(22): p. 21508-21514.

24. Snyder, R. and Hesselink, L., *MEASUREMENT OF MIXING FLUID-FLOWS WITH OPTICAL TOMOGRAPHY.* Optics Letters, 1988. **13**(2): p. 87-89.

25. Kang, M., Li, X., and Ma, L., *Calibration of Fiber Bundles for Flow and Combustion Measurements*, in *AIAA SciTech 2014, Paper AIAA-2014-0397*. 2014: National Harbor, MD.

26. Law, C.K., *Combustion Physics*. 2006, New York, USA: Cambridge University Press.

27. Ma, L., Li, X., Sanders, S.T., Caswell, A.W., Roy, S., Plemmons, D.H., and Gord, J.R., *50-kHz-rate 2D imaging of temperature and H< sub> 2</sub> O concentration at the exhaust plane of a J85 engine using hyperspectral tomography.* Optics Express, 2013. **21**(1): p. 1152-1162.

28. Cai, W. and Ma, L., *Comparison of Approaches Based on Optimization and Algebraic Iteration for Binary Tomography.* Computer Physics Communications, 2010. **181**(12): p. 1974-1981.

29. Cai, W. and Ma, L., *Improved Monte Carlo Model for Multiple Scattering Calculations.* Chinese Optics Letters, 2012. **10**(1): p. 012901.

Chapter 3 Analysis of 3D combustion measurements using CH-based tomographic VLIF (volumetric laser induced fluorescence)

(Published on Combustion and Flame, 182 (2017) 179-189)

Wenjiang Xu, Campbell D. Carter, Stephen Hammack, Lin Ma

Abstract

Recent results have experimentally demonstrated the feasibility of obtaining 3D (three-dimensional) combustion measurements using tomographic VLIF (volumetric laser-induced fluorescence), specifically of the CH radical, representing the flame surface. To elucidate the fundamental capabilities and limitations of the VLIF technique, this work reports an analysis of its performance in terms of signal level, size of the field of view (FOV) in 3D, and accuracy. Compared to the established PLIF (planar LIF) technique that uses a thin laser sheet to excite the target species in a plane, the VLIF technique uses a thick laser *slab* to excite the target species in a volume. As a result, the VLIF technique involves more performance metrics compared to PLIF, and the relationship between these metrics is also different from that in the PLIF technique. Therefore, both experimental and computational studies were conducted to analyze the performance metrics of VLIF. First, experiments were conducted on well-controlled flames to examine the relationship among excitation energy, signal level, and FOV in 3D. Second, based on these experimental data, numerical simulations were performed to benchmark the VLIF technique under a range of conditions. These results illustrate the relationship among signal level, 3D FOV, and accuracy and are expected to be valuable for the optimal design of the VLIF technique.

Keywords: Volumetric laser induced fluorescence, tomography

Introduction

The combustion diagnostic tool laser-induced fluorescence (LIF) enables researchers to obtain a variety of key flow and combustion parameters, ranging from species concentration [1-3], temperature [4], reaction progress [5], and mixture fraction [6]. In the past, LIF-based diagnostics have been largely established for measurements at a point, alone a line, or across a plane via PLIF (planar LIF) [7]. Most practical flows are turbulent and therefore inherently three-dimensional (3D) in space and dynamic in time [8, 9]. Therefore, there is a strong motivation to extend LIF to instantaneous 3D measurements. One possible strategy to enable 3D LIF involves a *scanning PLIF method* [10-16]. With this approach, one scans the probe laser sheet rapidly across multiple spatial locations and then records PLIF images sequentially at these locations, which are eventually compiled to form a 3D measurement. Another possible strategy involves combining tomography with LIF [17-24]. Here, 3D LIF measurements are obtained volumetrically—by expanding the laser beam to fill a target volume—without the need of scanning (and correspondingly this approach is termed VLIF, volumetric LIF). The volumetric LIF signal is projected and measured by cameras placed at different locations, and these projections are then used as the inputs to a tomography algorithm to reconstruct the 3D distribution of the target species.

The key performance metrics of LIF include signal level (directly related to measurement accuracy), size of the field of view (FOV), and spatial resolution. These performance metrics and their relationship have been examined and are well understood

for point, line, or planar LIF measurements [25-27] as well as for 3D LIF via the scanning method. For example, for the scanning PLIF method, signal level and FOV in the plane of the illuminating sheet should remain the same as the corresponding measurement via non-scanning PLIF. FOV in the depth direction is determined by the range of the scanning; spatial resolution in the plane of the illumination sheet should be approximately the same as the corresponding non-scanning PLIF, though some degradation will be incurred due to finite depth of field of the imaging system, determined by the scanning range, lens f-number, etc.

Experimental setup

The experimental setup is shown schematically in Figure 3-1(a) from the top view. This setup can be divided into three different major parts: a burner that produced the target flame for measurements, laser and optical systems that generated the excitation laser pulses, and the imaging systems that captured the VLIF signals.

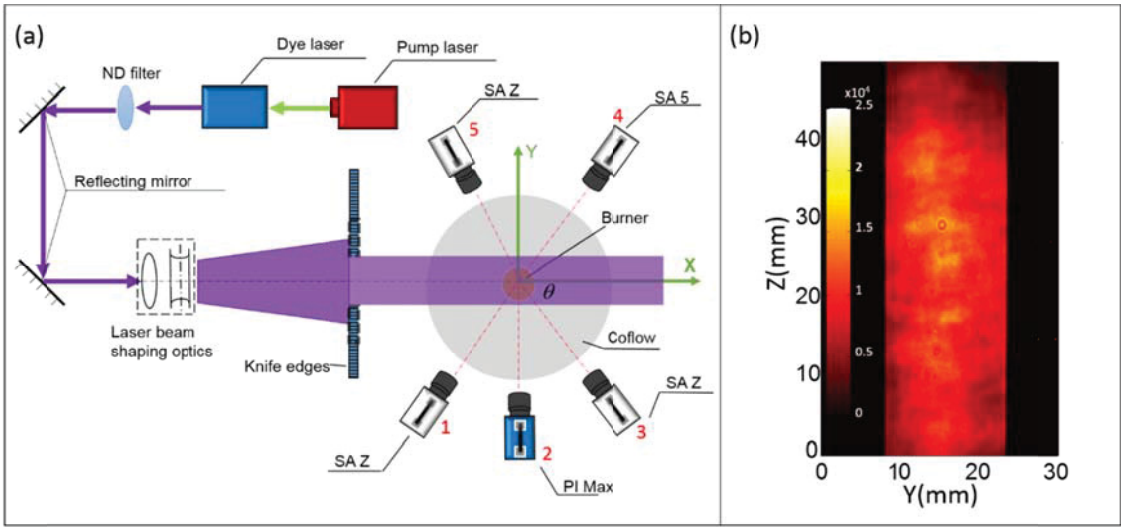

Figure 3-1. (a) Schematic of experimental setup, (b) Sample laser profile with slab thickness of 15 mm.

Two premixed CH_4-air burners were used in this work to produce premixed laminar and turbulent flames. The laminar burner consisted of a straight tube (5 mm ID) to generate a premixed Bunsen cone flame, an annular laminar pilot flame (18 mm ID) to anchor the central premixed flame, and an air co-flow (150 mm ID) to improve stability. The central burner operated on premixed CH_4 (chemically pure) and dry air at an equivalence ratio of 1.07 and a total flowrate of ~4.2 SLPM (standard liters per minute, referenced to 273 K). The turbulent burner was a rectangular Bunsen burner [28-31], with a width of 25.4 mm and a length of 50.8 mm. Two pilot flames were maintained at each side of the slot to anchor the turbulent flame and were operated near stoichiometric with a bulk velocity of about 0.37 m/s. The central turbulent burner was operated at an equivalence ratio of 1.07 and a total flowrate of ~500 SLPM, corresponding to a bulk velocity of ~8.5 m/s. This burner generated a turbulent flame with a height of about 150 mm. A turbulence-generating grid was installed in the central part to wrinkle the target flame, and the turbulent Reynolds number based on the integral scale was measured (by hot wire anemometry) to be 2,400 in the central region of the burner.

A dye laser system was used to generate the excitation pulses as shown in Figure 3-1(a). The pump laser was a 10-Hz Nd:YAG laser (Spectra- Physics GCR-170), whose output at 532 nm was used to pump a dye laser (Lumonics HD300 dye laser) employing a solution of DCM (Exciton) in methanol, producing a dye laser beam near 629 nm. The output from the dye laser was frequency doubled by an Inrad Autotracker III to generate the excitation pulses at the target wavelength of 314.415 nm. This wavelength was

chosen following the work described in ref. [32] to excite the overlapped $Q_2(6)$ and $Q_2(2)$ transitions from the CH $C^2\Sigma^+$ -- $X^2\Pi$ (v''= 0, v'= 0) band. The maximum pulse energy generated by this dye laser system was ~13 mJ/pulse, the pulse duration ~7 ns, and the linewidth ~0.1 cm^{-1}. A set of lenses were used to expand and shape the laser beam into a thick laser slab for the VLIF measurements. More specifically, the lenses used included a spherical concave lens with a focal length of -0.1 m, followed by a spherical convex lens with a focal length of 1 m. As a result, the 314.4-nm laser beam, with an initial diameter of ~2×5 mm, was expanded to a laser slab with thickness around 20 mm and height around 50 mm. Calibrated neutral density (ND) filters were used to adjust the delivered excitation energy in the VLIF measurements described below. A pair of knife edges clipped the excitation beam to control the thickness of the laser slab; the position of these knife edges, and thus the thickness of the laser slab, was adjustable. The intensity distribution of the resultant laser slab was measured at the probe region via a custom UV beam profiler, and the intensity distribution for a slab thickness of 15 mm is shown in Figure 3-1(b).

Based on the configuration of the burner and optical path, a Cartesian coordinate system was established such that the origin was defined at the center of the burner, the *X* axis was defined along the propagation direction of the laser, the *Y* axis was defined to be perpendicular to the propagation direction of the laser, and the *Z* axis was defined to be along the direction of the flow. The imaging system used to capture the VLIF signals included a total of five intensified cameras, as shown in Figure 3-1(a). Cameras 1, 3, and 5 were Photron model SA-Zs, and camera 4 was a Photron model SA-5, all equipped with the same intensifier (LaVision high speed IRO). Camera 2 was a PI-Max intensified

camera (Princeton Instruments). All cameras were aligned in the *X–Y* plane (i.e., in a coplanar fashion), and therefore their orientations were completely specified by θ, defined as the angle formed between the optical axis of each camera and the positive X axis in the anti-clockwise direction. All five cameras were equipped with the same UV lens (Cerco with f = 100 mm and f/2.8). A close-up lens (UV coated) was placed in front of the UV lens on each camera (with f = 200 mm, 300 mm, 200 mm, 250 mm, and 250 mm for cameras 1 through 5, respectively) to optimize the field of view and signal level. All lenses were fitted with a Schott UG-5 filter; furthermore, all cameras and intensifiers were synchronized with the laser at a frame rate of 10 Hz with an intensifier gate time of 100 ns. The models of cameras, lenses, and corresponding parameters were taken into consideration in the reconstruction. Prior to any measurement, a calibration target was placed on the burner to determine the orientation and location of the cameras with a view registration program [33]. The angular orientations of cameras 1 through 5 were found to be θ = 236°, 270°, 307°, 52°, and 114°, respectively, with uncertainly of ±0.5° [33].

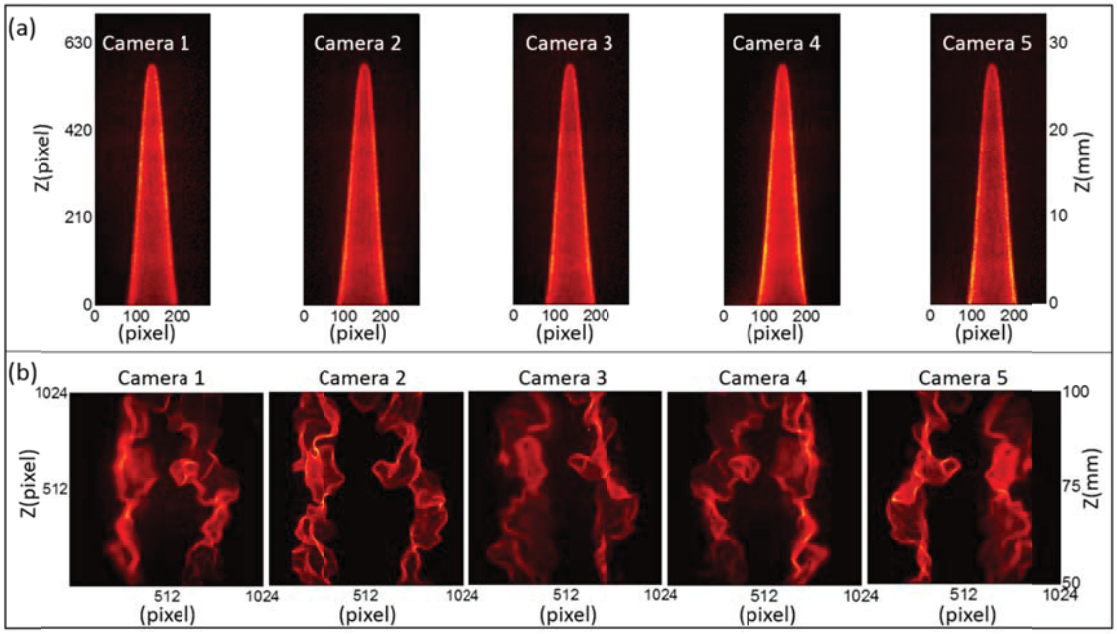

Figure 3-2. Sample projections of a laminar cone flame and a turbulent flame simultaneously captured from different viewing perspectives

To illustrate the nature of the experimental data, Figure 3-2 shows two sets of sample VLIF projections measured on a laminar (panel a) and a turbulent flame (panel b). These measurements were made with an excitation energy of ~6 mJ distributed nearly uniformly over a slab 10 mm thick (i.e., about half the pulse energy exiting the Autotracker was delivered to the probe region). Figure 3-2(a) shows the projections measured by all five cameras simultaneously on the laminar flame described above. The flame had an axially symmetric cone shape, with a base diameter of ~5 mm and an overall height of 28 mm. Due to its axial symmetry, the projections on the cameras were almost identical as seen in Figure 3-2(a) (and the differences were mostly caused by differences in the cameras and intensifiers). Each projection had a pixel resolution of 650 × 280, cropped from the original 1024×1024 image. Figure 3-2(b) shows the projections

measured from the turbulent flame. The current setup can only capture a FOV of 50 mm in the height direction, about one-third of the flame height of the turbulent flame. Figure 3-2(b) shows the measurements made 50 mm above the burner surface in the turbulent flame. These projections had a pixel resolution of 1024×1024. The data shown in Figure 3-2 serve as inputs into the model to be described in the following section for further analysis.

Model Development

This section describes the development of an approximate numerical model (relating fluorescence signal to various critical parameters) to enable analysis of the VLIF experimental data, such as those shown in Figure 3-3. The model includes two components, a model of the CH LIF signal and the tomographic algorithm. Although the analysis here is based on CH *C-X* transition, the model and some of the conclusions can be extended to VLIF measurements based on other species. In general the LIF signal (N_{LIF}) received by a given pixel over time t from an elemental volume (ΔV) can be expressed as

$$N_{LIF} = \frac{(\beta_f \Omega)}{4\pi} \int_{\Delta V} \int_0^{\infty} \sum_i A_i N_i dt dV \tag{1}$$

where β_f is the fluorescence detector efficiency and gain (counts or volts per incident photon), Ω is the solid angle formed by the voxel relative to the given pixel (equivalently the collection fraction of the voxel relative to the pixel), A_i is the fluorescence rate (1/s) for state i, and N_i is the number density (cm^{-3}) for radiating or excited state i. For a simple two-level model, the time-dependent number densities are given by (where subscripts 1 and 2 indicate the ground and excited states, respectively, and N_{CH} is the CH

number density)

$$\frac{dN_2(t)}{dt} = W_{12}N_1(t) - W_{21}N_2(t) - (Q + A_{21})N_2(t) \quad (2)$$

and

$$N_1(t) + N_2(t) = N_{CH} \quad (3)$$

where W_{12} and W_{21} are the respective rates for absorption and stimulated emission, Q is the excited-state quenching rate (in this case the sum of electronic quenching and predissociation rates), and A_{21} the spontaneous emission rate. The W_{ij} are related to the spectral laser irradiance (I_v) as such: $W_{ij} = I_v B_{ij} g/c$, where B_{ij} is the Einstein B coefficient, g the laser-transition overlap factor, and c the speed of light. In this work the rate equation for N_2 is solved and then N_2 is integrated in time for the total number of photons. This approach is superior to that using the steady-state equation because at high values of I_v, the temporal wings of the laser pulse contribute a linear portion to N_{LIF}, but the reader is cautioned that the assumption of a two-level system will necessarily limit the accuracy of the N_{LIF} model when transition saturation effects are strong. In the following text elaborating the VLIF model development, we use steady state solution to illustrate the role of key parameters for simplicity. At steady state one can derive the familiar form [25-27],

$$N_{LIF} = \Delta V \cdot \frac{\beta_f \Omega}{4\pi} \cdot [\frac{B_{12}}{B_{12} + B_{21}} \cdot \frac{A_{21}}{1 + \frac{(A_{21} + Q)c}{(B_{12} + B_{21})(I_v \cdot g)}} \cdot \Delta t] \cdot N_{CH} \quad (4)$$

where the Einstein coefficients are adopted from LIFBASE [34], with B_{12} and B_{21} = 8.5×10^{18} $m^3J^{-1}s^{-2}$, and A_{21} = 9.04×10^6 s^{-1}, while the overlap factor g is estimated to be 0.24 based on the laser linewidth (0.1 cm^{-1}) and the estimated transition linewidth. The

quenching rate is assumed to be constant, since CH radicals exist in a thin zone near flame front, and equal to $1\times10^{9}\ s^{-1}$; considering the lack of CH quenching rate data [35, 36], the quenching rate of CH is assumed to be similar to that for A-state OH.

The above equation describes the LIF signal that is received by a given pixel from one voxel in the measurement region. Then the ultimate VLIF signal received by a given pixel is obtained by integration over the entire measurement region, shown in Eq. (5) below as a summation when the measurement region is discretized in a series of voxels:

$$P(r,\theta,\phi)=\sum_{x_i,y_i,z_i}\Delta V\cdot\frac{\beta_f\Omega(x_i,y_i,z_i;r,\theta,\phi)}{4\pi}\cdot I(x_i,y_i,z_i)\cdot N_{CH}(x_i,y_i,z_i) \tag{5}$$

where $P(r,\ \theta,\ \phi)$ represents the VLIF signal received by a pixel on a camera, whose location and orientation are specified by its distance to the origin (r), azimuth angle (θ), and inclination angle (ϕ); and ($x_i,\ y_i,\ z_i$) the spatial coordinates of the i^{th} voxel. Eq. (5) essentially states that the VLIF signal on a given pixel is a summation of the LIF photons contributed from all voxels in the measurement region. Here I denotes the terms within the bracket in Eq. (4), and it depends solely on the irradiance of the excitation pulse when Q is a constant. As a result, the spatial dependence of I is determined by the spatial distribution of the excitation pulse (as shown in Fig. 1b). Furthermore, absorption of the laser pulse by CH is negligible, due to the fact that CH radicals only exist in a thin layer near the flame front at low concentration (of order 10 ppm); likewise, fluorescence trapping is also negligible. Therefore, under this formulation, the VLIF signal depends on the concentration of the target species (i.e., N_{CH} in this work) linearly. Note that under cases where significant absorption or fluorescence trapping occurs, I also depends on the distribution of the target species, making the LIF problem nonlinear, and in this case the VLIF problem would need to be modeled and solved differently [19, 37].

One major difference and complication of VLIF compared to PLIF involves the spatial variation of Ω, which, as emphasized in Eq. (5), depends on the location and orientation of the camera (r, θ, ϕ), and also the location of the voxel (x_i, y_i, z_i). In PLIF measurements, such spatial variation is typically small and ignored, due to the relatively small thickness of the laser sheet and the fact that only one camera is used at a normal angle. In VLIF measurements, however, such spatial variation becomes significant and needs to be considered. Note that such spatial variation of Ω is equivalent to the concept of the point spread function (*PSF*) [38]. In this work Ω is computed with a combination of a Monte Carlo and ray tracing technique, as detailed in refs. [32, 39]. After obtaining Ω, Eq. (5) can either be used to calculate the signal of VLIF measurements with given N_{CH} (the so-called forward problem) or solved to obtain the 3D reconstruction of N_{CH} with given projections (the so-called inverse problem), as will be discussed in the following section.

Assessment of VLIF signal level

In this section our model is applied to study the forward problem, more specifically, the dependence of the signal level on excitation pulse energy and dimension of the measurement volume. Before doing so, the accuracy and validity of the model was examined through comparison to controlled experiments as shown in Figure 3-3. First, the excitation irradiance was varied with a fixed volume (3a), and then measurement

volume (3b) was varied with a fixed excitation irradiance.

More specifically, Figure 3-3(a) shows the projections measured by one camera (camera 2) sequentially on a laminar cone flame under increasing excitation pulse energies with the laser slab thickness fixed at 10 mm. These measurements were designed to study the VLIF signal level produced within a fixed measurement volume but varying excitation pulse energy (or spectral irradiance). As can be seen in Figure 3-3(a), the VLIF signal level gradually increases from left to right, corresponding to respective excitation pulse energy of about 0.06, 0.18, 0.3, 0.6, 1.8, 3.0, and 6.0 mJ (controlled via the ND filters). Note that the leftmost image shows 3× of the actual signal level, just to make the image visible using the same color scale as employed with the other images. Figure 3-3(b) shows the projections measured sequentially on the same camera with increasing laser slab thicknesses (controlled by adjusting the positions of the knife edges) but fixed excitation irradiance. The measurement volume was adjusted by moving the knife edges, and the excitation irradiance was fixed by keeping the laser output constant at 6 mJ/pulse (with no ND filter used). Note that for this measurement, the actual laser energy used to illuminate the flame varied, since the fraction of the total energy transmitted by the knife edges varied; as the spatial distribution of laser energy was relatively uniform (resulting from the "over expansion" of the 314.4-nm beam relative to the knife-edge aperture, as indicated in Fig. 1), the laser irradiance was nearly constant, independent of the slab thickness. Here, the thickness of the measurement volume/slab increased from 1 mm for the leftmost image to 7 mm (rightmost image) with an increment of 1 mm. Note that the measurement volume expanded from one edge of the flame to the other edge (i.e., it did not expand symmetrically from the center of the flame), which is best illustrated by the

leftmost image taken at 1 mm, where only a small portion of the flame near its edge was illuminated and imaged.

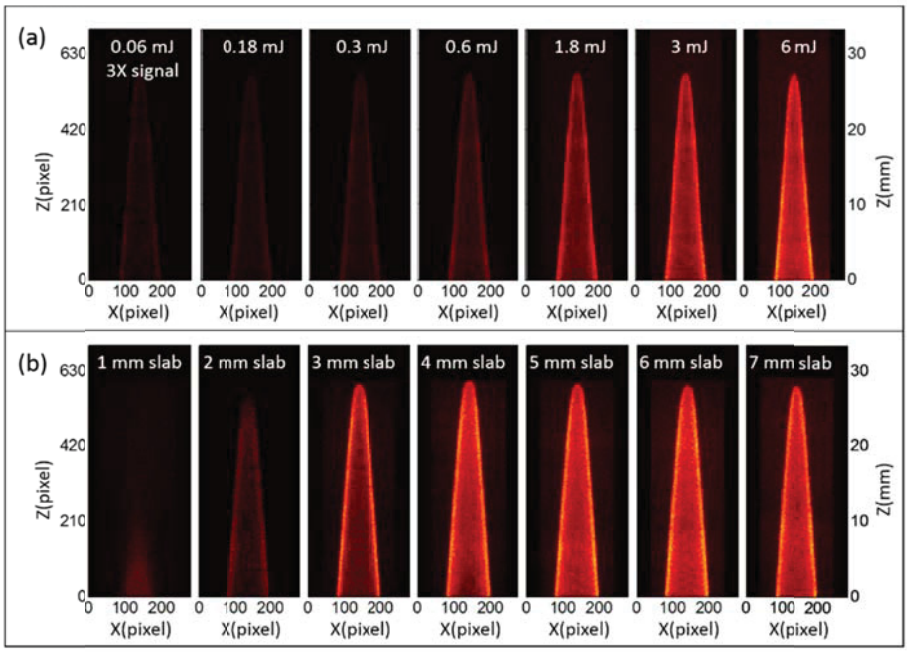

Figure 3-3. Sample projections of a laminar cone flame under different conditions taken by camera 2. (a) Varying spectral irradiance of excitation laser pulses under constant laser slab thickness, (b) Varying laser slab thickness under constant spectral irradiance of excitation laser pulses.

The model described in Section 3 was applied to simulate these measurements, and the comparison of the simulation and experimental results is shown in in Figure 3-4 and Figure 3-5. The simulation was performed using inputs identical to the experimental conditions (e.g., a phantom cone flame identical to the experimental flame was created and used as the input). Applying the VLIF model together with the program to take account of varying Ω, the projections expected on each camera were simulated. Figure 3-4 and Figure 3-5 show the average VLIF signal level determined from the simulated and experimental projections, and here the average signal was defined as the average number of LIF photons received per pixel on the projection. Note that the analysis of the

signal level in Section 3 was based on a steady-state assumption primarily for the sake of clarity in illustrating the relationship between the key parameters. An analysis considering time-dependence of the LIF process led to similar relationship as derived in Section 3, and the simulations shown here took such time-dependence into consideration.

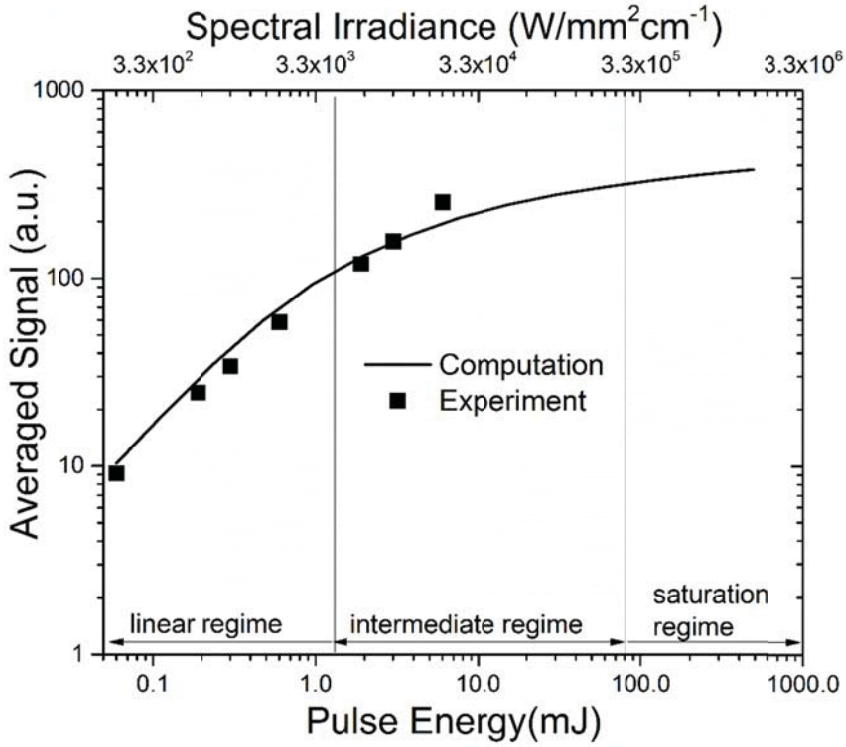

Figure 3-4. Variation of VLIF signal level with respect to excitation pulse energy obtained from experiments and computations.

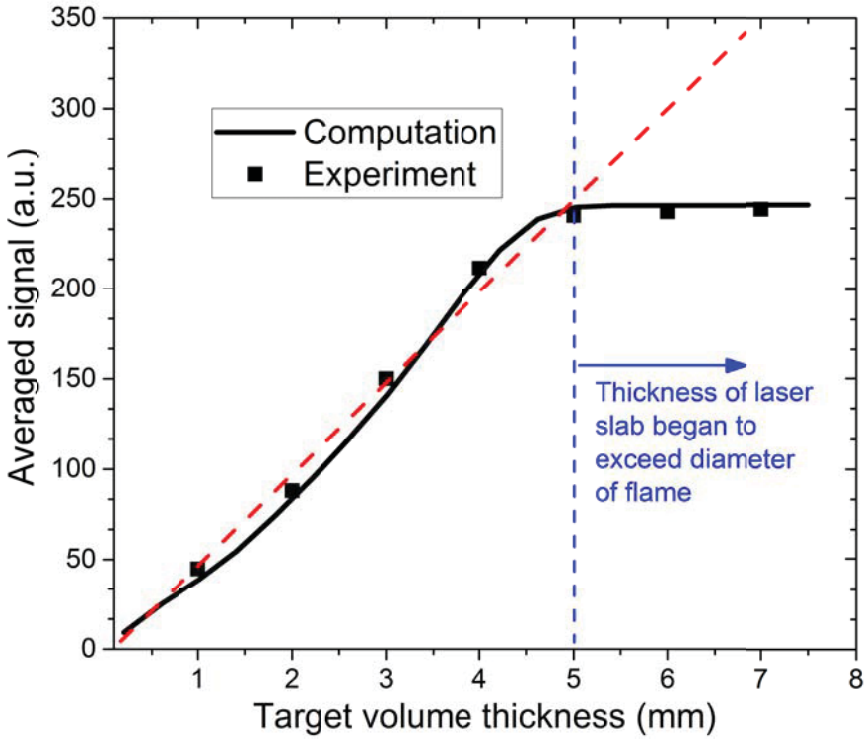

Figure 3-5. Variation of VLIF signal level with respect to laser slab thickness obtained from experiments and computations.

Several observations can be made from such comparison. First, the experimental signal levels were scaled by the same factor (to account for factors such the cameras' conversion of optical signal to electrical signal and signal loss due to reflection on surfaces of optical components, etc.). And as seen, this same factor was able to collapse all experimental data to good agreement with simulations, which provides confidence for use of the model over the range of I_v values employed and reasonable confidence for extrapolation of I_v values too (but with the caveat noted above regarding limitations of the two-level model). Figure 3-4 shows the signal level under increasing excitation energy in a fixed measurement volume, resulting in increasing irradiance (the top axis of Figure 3-4 shows the spectral irradiance, defined based on the cross sectional area of the laser slab). As seen, the VLIF signal increases in a similar fashion as the traditional PLIF signal [7, 25], clearly displaying linear, intermediate, and saturation regimes. Here, the

separation of these regimes was rather arbitrarily chosen to be at spectral irradiance of 3×10^3 and 2×10^5 W/mm^{2}cm^{-1} as shown. In summary, Figure 3-4 shows that within a fixed measurement volume, the average VLIF signal increases with respect to excitation irradiance in a fashion similar to a PLIF signal. The comparison shown in Figure 3-5, on the other hand, illustrates a fundamental difference between the VLIF and PLIF signals, due to the integrating nature of the VLIF signal. Figure 3-5 shows that the average signal level increases almost linearly with respect to the laser slab thickness (the red dashed line was plotted to aid the visual interpretation of the linear trend). Such linear increase stopped at a slab thickness of 5 mm only because the thickness of the laser slab began to exceed the diameter of the target flame, and the VLIF signal remained almost constant beyond this point.

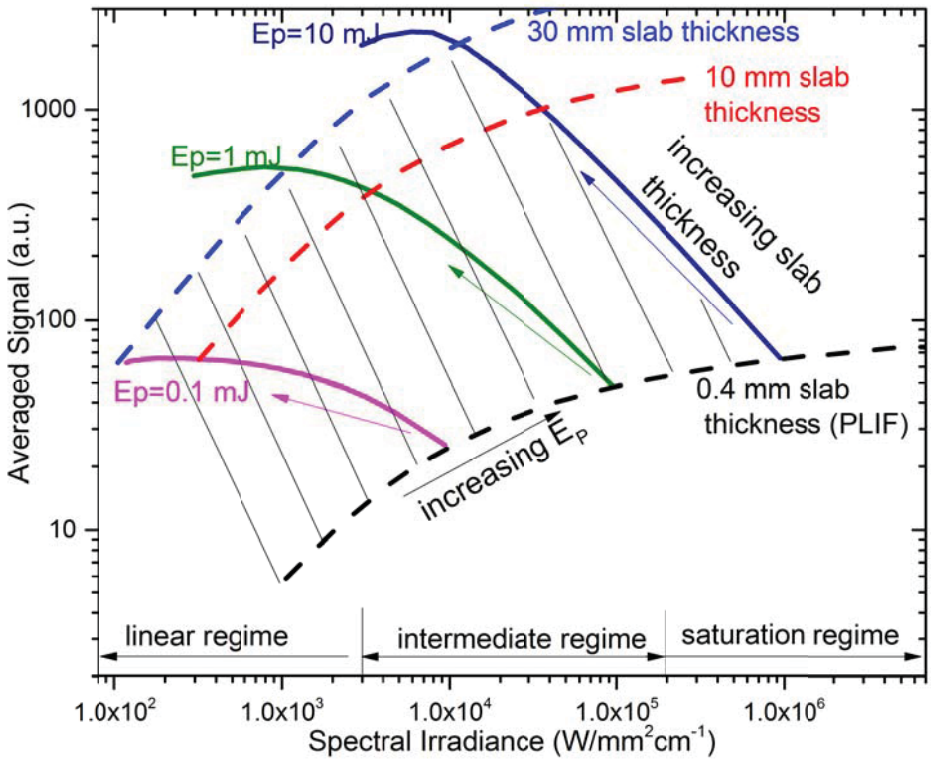

Figure 3-6. Simulated VLIF Signal level under various excitation pulse energies and laser slab thicknesses.

After the comparison and validation of the VLIF model against two controlled experiments, it was applied to predict the capabilities and limitations of VLIF signal over a range of parameters as shown in Figure 3-6. First, the dashed lines in Figure 3-6 show the VLIF signal increases with respect to irradiance at three laser slab thicknesses (0.4 mm, 10 mm, and 30 mm, respectively). The result corresponding to a slab thickness of 0.4 mm corresponds approximately to that for PLIF. The VLIF signal again varies in a fashion similar to the PLIF signal, displaying distinctly linear, intermediate, and saturation regimes. Also note that at constant irradiance, the VLIF signal increases with respect to laser slab thickness due to the integrating effects as noted vis-à-vis Figure 3-5. The phantom flame used in the simulations shown here in Figure 3-6 was set to be large enough so the laser slab never exceeded the flame dimension (whereas the laser slab thickness exceeded the flame after 5 mm as shown in Figure 5).

In addition, the three solid lines show the VLIF signal at three constant excitations pulse energies (E_P = 0.1, 1, and 10 mJ) with varying laser slab thicknesses. Note that these calculations were made under the assumption that the same amount of excitation energy was used and distributed within a varying slab thickness, hence resulting in varying spectral irradiance. This assumption was made to simulate experimental performance under an ideal condition where the laser pulse energy available (either 0.1, 1, or 10 mJ) can always be used for the VLIF measurement at different slab thicknesses (for example, by applying different optics to focus all the laser pulse energy into a slab with the desired thickness). Such assumption is only partially valid due to practical limitations, such as the difficulty of focusing the laser pulse energy into an ideal slab with

various thicknesses, and therefore the results shown here represent an estimation of the VLIF signal with an optimal use of the pulse energy available. Under the current scenario, one might expect the signal level to decrease as laser slab thickens because the laser irradiance decreases. However, as seen, the signal level actually remains almost constant in the linear regime (see the line corresponding to E_P = 0.1 mJ) and first increases then decreases in the intermediate or saturation regime (see the lines corresponding to E_P = 1 and 10 mJ). The signal remains almost constant in the linear regime because 1) the signal emitted per volume (i.e., N_{LIF}) decreases linearly with respect to slab thickness, 2) the integrating volume increases linearly with respect to slab thickness, and 3) the above two effects offset each other. In the intermediate and saturation regime, however, the signal first increases because N_{LIF} decreases sub-linearly with respect to slab thickness while the integrating volume increases linearly, resulting in a net increase in signal level. The subsequent decrease in signal level as the laser slab further expands is caused by the change in Ω. As discussed in Section 3, under a given set of imaging optics (set to be the same as those used in the experiments in these simulations), Ω varies from voxel to voxel, and this variation plays a role in the overall signal level. When the laser slab thickness varies in a relatively narrow range, the variation in Ω is relatively small, and the change in signal level is dominated by N_{LIF} and the integrating volume. When the laser slab thickness varies in a sufficiently wide range, the variation in Ω correspondingly increases and manifests its roles as shown by the left portions of the lines corresponding to E_P = 1 and 10 mJ. Besides illustrating the nature of the VLIF signal level and its differences compared to PLIF signal dependence, Figure 3-6 also helps to map out the potential applicable range of the VLIF technique for a given set

of experimental conditions. For example, the hatched area displays the possible signal level obtained with VLIF in a measurement volume up to 30 mm thick and an excitation pulse energy up to 10 mJ.

Assessment of reconstruction accuracy

With the ability to simulate the VLIF signal enabled by the model described above, the accuracy of the 3D tomographic reconstruction based on the VLIF signals can be assessed. In our past work [21], the accuracy of 3D VLIF reconstructions was assessed using a stable laminar flame, due to the difficulty of creating controlled turbulent flames with known patterns. With the VLIF model developed here, the reconstruction accuracy can be numerically assessed for arbitrary flames, such as that shown in Figure 3-7, which shows two sets of VLIF projections (from the five intensified cameras) employing the turbulent Bunsen burner. More details of these measurements are provided in ref. [31]. Figure 3-7 shows the VLIF projections measured at two different laser slab thicknesses: a thickness of 10 mm in panel (a) and (b) (E_p = 6 mJ) and a thickness of 15 mm in panel (c) and (d) (E_p = 9 mJ), respectively. The same excitation irradiance (approximately) was maintained for both sets of measurements. As mentioned in Section 2, the overall height of the flame was ~150 mm, and the FOV of the imaging systems was ~50 mm in the z direction. Thus, the VLIF projections shown in Figure 3-7 were captured sequentially by changing the height of the burner (which was mounted on a 3-axis translation stage). These projection images again illustrate the increased signal level with respect to the laser slab thickness, due to the integrating nature of the VLIF signal. Also, Figure 3-7 (c) and (d) show more complicated structure than panel (a) and (b), illustrating that more flame structures were captured and integrated with a thicker laser slab.

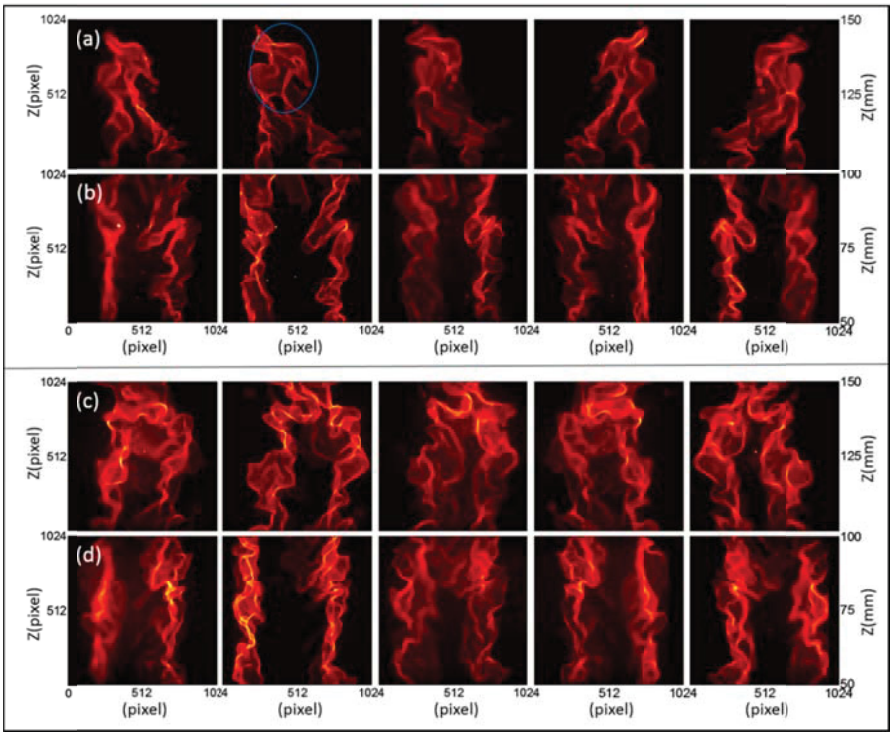

Figure 3-7. Projection measurements of turbulent flames with slab thicknesses of 10 mm (panels (a) and (b)) and 15 mm (panels (c) and (d)).

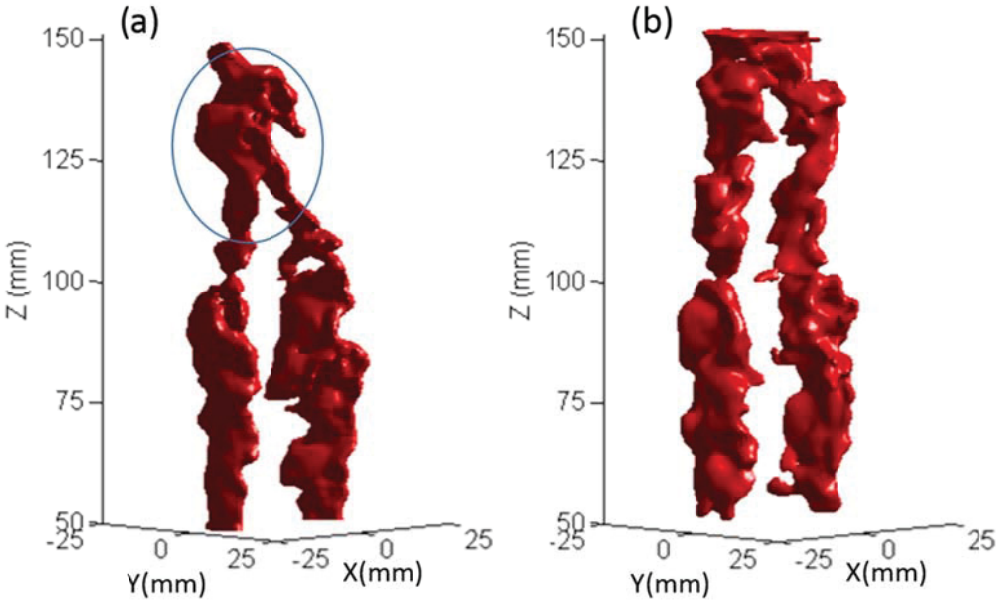

Figure 3-8. 3D reconstruction of turbulent flames with (a) 10 mm laser slab (b) 15 mm laser slab. Flame surface is discontinuous at Z=100 mm, since the data shown is a merging of two independent sections.

Using the projections shown in Figure 3-7 as inputs, a 3D reconstruction of the turbulent flame can be obtained as shown in Figure 3-8. Figure 3-8(a) shows the 3D reconstruction obtained using the projections shown in the Figure 3-7(a) and (b), i.e., with a laser slab thickness of 10 mm; and Figure 3-8(b) using the projections shown in Figure 3-7(c) and (d) with a laser slab thickness of 15 mm. The number of voxels (i.e., unknowns to be solved) used in the reconstruction was 128×128×128 (i.e., about 2M), and the number of pixels (i.e., equations) available from each projection picture was 1024 by 1024 (i.e., about 1M per projections) leading to a total of ~5M equations, resulting in an overly determined system. A visual examination of the projections and the reconstruction suggest that the reconstruction correctly captured the instantaneous structure of the turbulent flame at both overall and detailed levels (e.g., by comparing the feature highlighted in the oval shown in Figure 3-7(a) and Figure 3-8(a)). With the VLIF model developed above, the reconstruction quality can be assessed more quantitatively. Figure 3-9 shows the simulated VLIF signal of the projections at various laser slab thicknesses for the target turbulent flames under fixed excitation irradiance, obtained using phantoms created to duplicate the flames shown in Figure 3-8(b). As seen again, the average LIF signal increases with respect to the thickness of the laser slab, under the scenario that the laser beam is over-expanded and the irradiance at the knife edges a constant. Figure 3-9 also shows two experimental data points obtained from the measurements shown in Figure 3-7. These data points were normalized by a common factor, and the agreement between the simulations and the experimental data is consistent with those discussed earlier.

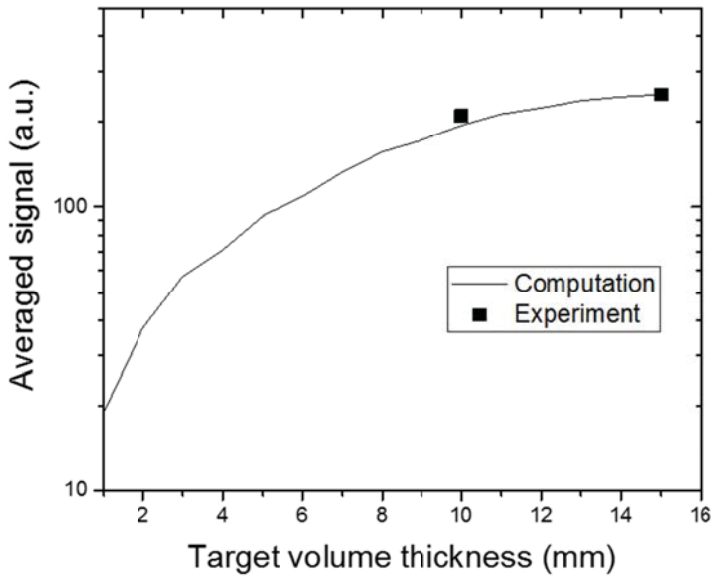

Figure 3-9. VLIF signal level for turbulent flames vs. laser slab thickness.

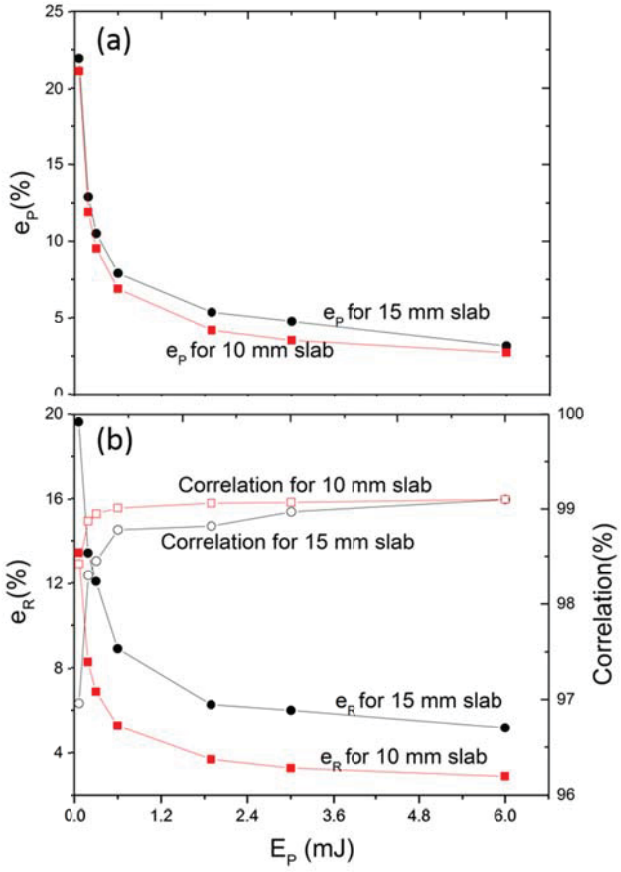

Figure 3-10. Projection error (e_P) and reconstruction accuracy (e_R) of turbulent flames, assuming two slab thicknesses (10 and 15 mm).

With the signal level simulated, the 3D reconstruction quality can now be assessed, and the results are shown in Figure 3-10. The assessment was performed in two steps. In the first step, projection measurements were simulated using the VLIF model described and validated above. Similar to the comparison of the VLIF model and the experimental results discussed earlier, here the simulation results were scaled by the same β_f factor (to account for factors such the cameras' conversion of optical signal to electrical signal and signal loss due to reflection on surfaces of optical components, etc.). Figure 3-10a shows the uncertainty (e_P) in the projection measurements based on flame phantoms resembling those shown in Figure 8. The simulations were made employing two laser slab

thicknesses, again to simulate the experimental conditions used in Figure 3-8. The projection error (e_P) here is defined as the following:

$$e_P = \frac{\sum | P_{Noisy} - P_{NF} |}{\sum P_{NF}} \tag{5}$$

where P_{Noisy} represents the projections with measurement noise, P_{NF} the ideal noise-free projection, and the summation runs over all the pixels of the measurements. Therefore, the e_P defined here quantifies the overall noise level of the projection measurements. In practice, various kinds of noise can be present to contaminate the projections. However, only shot noise is considered in these simulations because the goal of this work is to assess the performance limit of the VLIF technique. Ignoring other noise sources and only considering the shot noise provides a "best case" of the measurement accuracy. As a result, Figure 3-10(a) shows that the projection error decreases with increasing laser excitation energy, in accordance with the result of signal level shown in Figure 3-6 and reflecting the trend of decreasing shot noise at increasing LIF signal level. In this work, the lowest e_P was estimated to be ~ 4% according to the results shown in Figure 3-10(a), when the maximum excitation energy of 6 mJ was used.

The second step of the assessment involved performing the tomographic reconstruction using the simulated projections obtained in the first step. The error in the projection (e_P) propagates in the tomographic reconstruction process, which is eventually reflected as an error in the reconstruction. To quantify the reconstruction error, it was compared to the phantom by two metrics, the first being an overall reconstruction error (e_R),

$$e_R = \frac{\sum | F_{Recon} - F_{Phantom} |}{\sum F_{Phantom}} \tag{6}$$

where F_{Recon} represents the reconstruction obtained, $F_{Phantom}$ a phantom created numerically to simulate the 3D distribution of CH concentration expected in the experiments, and the summation sign runs over all the voxels in the measurement domain. This metric therefore quantifies the overall discrepancy between the reconstruction and the phantom distribution. The second metric was a correlation between the reconstructed and phantom distributions. The use of the correlation metric in addition to e_R was motivated by the consideration that e_R may not provide a complete characterization of the reconstruction accuracy. As an example, consider a case where the reconstruction and phantom distributions are exactly the same in shape but are offset from each other spatially. In this case, e_R could be large while the reconstruction is still completely accurate when only the shape of the distribution is concerned (for example, when the measurement is used to calculate flame surface area or curvature). Therefore, the use of the correlation could provide additional information to better interpret the accuracy of the reconstruction. Figure 3-10(b) shows e_R and the correlation at different excitation pulse energies calculated from the computational results. As seen, with the increase of excitation pulse energy (and hence increasing signal level and decreasing e_P), e_R decreased and the correlation approached 1. With the maximum excitation pulse energy of 6 mJ used in this work, the reconstruction error e_R was less than 4% for an slab thickness of 10 mm and about 5% for a slab thickness of 15 mm. The reason for such difference in reconstruction accuracy was due to the fact that with a thicker laser slab, more flame structures are captured and the reconstruction becomes more challenging. Such increased challenge is due to the generic difficulty associated with multi-scale and multi-dimensional problems. Resolving features of a given (i.e., fixed) length scale in a

larger volume is generically more difficult than resolving them in a smaller volume. Extending multidimensional measurements to a larger volume will require either reducing the resolution of the measurement (i.e., to only resolve larger length scales) or increasing the number of cameras to obtain more projections. To maintain the same level of reconstruction accuracy in a larger measurement volume, possible approaches to improve the accuracy include the use of more cameras to provide more information in the tomographic reconstruction and/or more advanced reconstruction algorithms that better utilize the projection information. Also, as seen, with this maximum excitation pulse energy, the correlation between the reconstruction and the phantom was almost the same and was above 99% for both the 10-mm and 15-mm laser slab thickness, illustrating the utility of the correlation as another assessment metric.

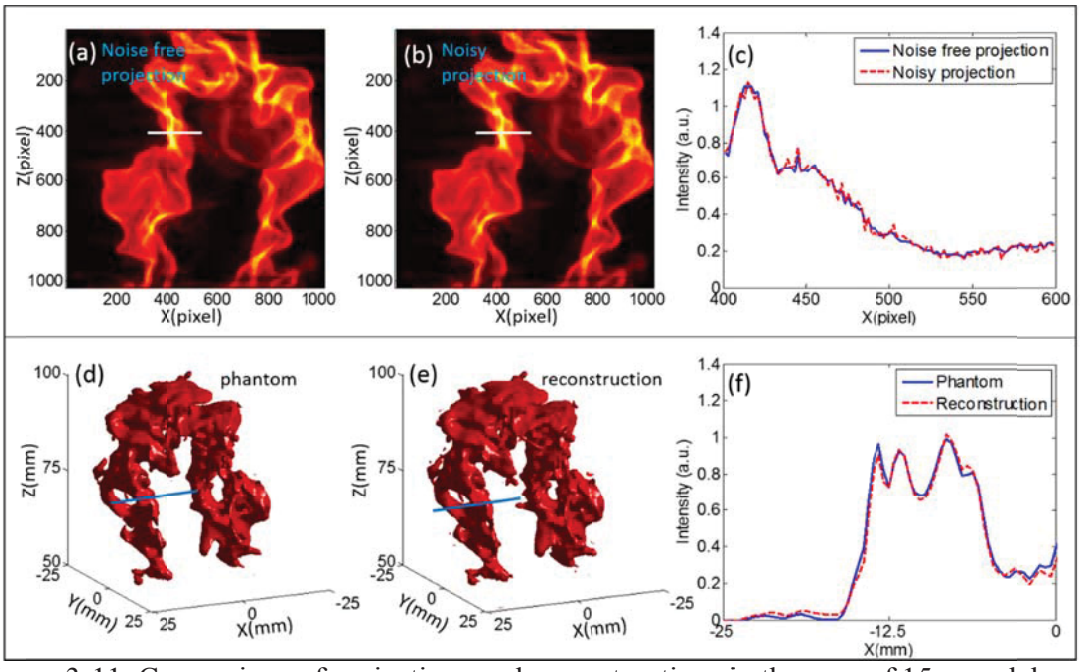

Figure 3-11. Comparison of projections and reconstructions in the case of 15 mm slab and an excitation energy of 3 mJ. (a) Noise free projection, (b) noisy projection, (c) comparison of noise free and noisy projection along a line, (d) 3D phantom, (e) 3D reconstruction, and (f) comparison of the phantom and reconstruction along a line.

Figure 3-11 shows some of the intermediate results used to obtain Figure 10 to better illustrate the meaning of the errors used in the above analysis and their effects. These intermediate results from the case with a slab thickness of 15 mm and an excitation pulse energy of 3 mJ, with a projection error e_P of 5.4% and a reconstruction error e_R of 6.3% as seen on Figure 10. First, Figure 3-11(a) and (b), respectively, show a noise-free projection (i.e., P_{NF}) and a noisy projection (i.e., P_{Noisy} at the given excitation energy and slab thickness). The average difference as defined in Eq. (5) between Figure 3-11(a) and (b) is 5.4%. Figure 3-11(c) compares the noise-free and noisy projections along a line (the white line shown in Figure 3-11(a) and (b)). This particular line was chosen such that the difference between the noisy and noise-free projections along it (which was 5.6%) is close to the overall e_P = 5.4% to illustrate the magnitude of such projection error. Similar to the comparison of the projections in Figure 3-11(a)-(c), Figure 3-11(d), (e) and (f), respectively, show the phantom (i.e., $F_{Phantom}$), the reconstruction (F_{Recon}), and the comparison of the phantom and reconstruction along a line (the blue line shown in panel d and e). The reconstruction error (i.e., e_R) as defined in Eq. (6) was 6.3% for this case. This particular line was again chosen such that the difference between the phantom and the reconstruction along it (which was 6.2%) is close to the overall e_R = 6.3% to illustrate the magnitude of such reconstruction error. As seen in Figure 3-11(f), a reconstruction error near 6% represents close agreement between the reconstruction and the phantom, illustrating the ability to resolve 3D flame structures via VLIF.

Besides the above simulation presented in this section, we are attempting other

validation methods in our ongoing work. For example, one other validation approach involves a direct comparison between VLIF and PLIF measurements. The concept is to perform VLIF measurements and PLIF simultaneously and then to compare the PLIF directly against a 2D cross-section of the VLIF at the same planar location where the PLIF is taken, with preliminary results reported in [40].

Conclusion

This work reports an experimental and computational study of the fundamental capabilities and limitations of the volumetric laser-induced fluorescence (VLIF) technique for three-dimensional (3D) combustion measurements (i.e., tracking the flame front) based on the CH radical. The goal of this work was to map out the performance limits of VLIF in terms of signal level, size of the field of view (FOV) in 3D, and accuracy. To accomplish this goal, experiments were performed on laminar and turbulent flames under various excitation pulse energies and laser "slab" thicknesses. These measurements were then used to validate a VLIF model, which considered a simple time-dependent two-level LIF model of the CH *C-X* transition and the position-dependent collection efficiency of the LIF signal. After verifying reasonable agreement between the experimental and modeling results, the model was then used to assess the capabilities and limitations of the VLIF technique. The results illustrate that the VLIF technique, due to its volumetric nature, involves more performance metrics than its 2D equivalent (planar LIF or PLIF), and the relationship between these metrics differ between VLIF and PLIF. Particularly, the VLIF signal level behaves differently and can remain constant or even increase with decreasing irradiance due to spatial integrating effects. The model also

enables the assessment of the error of the 3D measurements, which should enable the user to optimize the setup and maximize 3D information while minimizing errors. These results show that an overall reconstruction error of ~5% and correlation better than 99% can be obtained in a reasonably large volume (50×50×15 mm in this work) with an excitation energy under 10 mJ for CH *C-X* probing under the shot-noise-limited assumption, illustrating the capability and accuracy that can be expected when commercially available laser equipment is used for VLIF measurements.

Acknowledgement

This work is supported by the U.S. Air Force Office of Scientific Research (AFOSR, grant FA9550-14-1-0386), and a 2015 U.S. Air Force Summer Faculty Fellowship. This research was performed while a coauthor held an NRC Research Associateship award at the Air Force Research Laboratory (AFRL). We are also grateful to Dr. Tonghun Lee (University of Illinois) and Dr. James R. Gord (AFRL) for the loan of equipment.

References

1. Berg, P.A., Hill, D.A., Noble, A.R., Smith, G.P., Jeffries, J.B., and Crosley, D.R., *Absolute CH concentration measurements in low-pressure methane flames: Comparisons with model results.* Combustion and flame, 2000. **121**(1): p. 223-235.

2. Luque, J. and Crosley, D., *Absolute CH concentrations in low-pressure flames measured with laser-induced fluorescence.* Applied Physics B, 1996. **63**(1): p. 91-98.

3. Kristensson, E., Li, Z., Berrocal, E., Richter, M., and Aldén, M., *Instantaneous 3D imaging of flame species using coded laser illumination.* Proceedings of the Combustion Institute.

4. Seitzman, J.M., Kychakoff, G., and Hanson, R.K., *Instantaneous temperature field measurements using planar laser-induced fluorescence.* Optics Letters, 1985. **10**(9): p. 439-441.

5. Tanahashi, M., Murakami, S., Choi, G.-M., Fukuchi, Y., and Miyauchi, T., *Simultaneous CH–OH PLIF and stereoscopic PIV measurements of turbulent premixed flames.* Proceedings of the Combustion Institute, 2005. **30**(1): p. 1665-1672.

6. Zhao, Y., Tong, C., and Ma, L., *Demonstration of a New Laser Diagnostic Based on Photodissociation Spectroscopy for Imaging Mixture Fraction in a Non-premixed Jet Flame.* Applied Spectroscopy, 2010. **64**(4): p. 377-383.

7. Hanson, R., Seitzman, J., and Paul, P., *Planar laser-fluorescence imaging of combustion gases.* Applied Physics B, 1990. **50**(6): p. 441-454.

8. Barlow, R.S., *Laser diagnostics and their interplay with computations to understand turbulent combustion* Proceedings of the Combustion Institute 2007. **31**(1): p. 49-75.

9. Nathan, G., Kalt, P., Alwahabi, Z., Dally, B., Medwell, P., and Chan, Q., *Recent advances in the measurement of strongly radiating, turbulent reacting flows.* Progress in Energy and Combustion Science, 2012. **38**(1): p. 41-61.

10. Kychakoff, G., Paul, P.H., van Cruyningen, I., and Hanson, R.K., *Movies and 3-D images of flowfields using planar laser-induced fluorescence.* Applied Optics, 1987. **26**(13): p. 2498-2500.

11. Nygren, J., Hult, J., Richter, M., Aldén, M., Christensen, M., Hultqvist, A., and Johansson, B., *Three-dimensional laser induced fluorescence of fuel distributions in an HCCI engine.* Proceedings of the Combustion Institute, 2002. **29**(1): p. 679-685.

12. Cho, K.Y., Satija, A., Pourpoint, T.L., Son, S.F., and Lucht, R.P., *High-repetition-rate three-dimensional OH imaging using scanned planar laser-induced fluorescence system for multiphase combustion.* Applied Optics, 2014. **53**(3): p. 316-326.

13. Miller, V.A., Troutman, V.A., and Hanson, R.K., *Near-kHz 3D tracer-based LIF imaging of a co-flow jet using toluene.* Measurement Science and Technology, 2014. **25**(7): p. 075403.

14. Wellander, R., Richter, M., and Aldén, M., *Time-resolved (kHz) 3D imaging of OH PLIF in a flame.* Experiments in Fluids, 2014. **55**(6): p. 1-12.

15. Yip, B., Schmitt, R.L., and Long, M.B., *Instantaneous three-dimensional concentration measurements in turbulent jets and flames.* Optics Letters, 1988. **13**(2): p. 96-98.

16. Yip, B., LAM, J., Winter, M., and LONG, M., *Time-resolved three-dimensional concentration measurements in a gas jet.* Science, 1987. **235**(4793): p. 1209-1211.

17. Halls, B.R., Thul, D.J., Michaelis, D., Roy, S., Meyer, T.R., and Gord, J.R., *Single-shot, volumetrically illuminated, three-dimensional, tomographic laser-induced-fluorescence imaging in a gaseous free jet.* Optics Express, 2016. **24**(9): p. 10040-10049.

18. Ma, L., Lei, Q., Ikeda, J., Xu, W., Wu, Y., and Carter, C.D., *Single-shot 3D flame diagnostic based on volumetric laser induced fluorescence (VLIF).* Proceedings of the Combustion Institute, 2017. **36**(3): p. 8.

19. Wu, Y., Xu, W., Lei, Q., and Ma, L., *Single-shot volumetric laser induced fluorescence (VLIF) measurements in turbulent flows seeded with iodine.* Optics Express, 2015. **23**(26): p. 33408-33418.

20. Benjamin, R.H., James, R.G., Naibo, J., Mikhail, S., Sukesh, R., and Terrence, R.M., *High-speed three-dimensional tomographic measurements for combustion systems*, in *32nd AIAA Aerodynamic Measurement Technology and Ground Testing Conference*. 2016, American Institute of Aeronautics and Astronautics.

21. Ma, L., Xu, W., Lei, Q., Ikeda, J., and Carter, C., *Single-Shot 3D Flame Imaging Using CH-Based VLIF (Volumetric Laser Induced Fluorescence)*, in *32nd AIAA Aerodynamic Measurement Technology and Ground Testing Conference*. 2016, American Institute of Aeronautics and Astronautics.

22. Wu, Y., Lei, Q., Xu, W., and Ma, L., *5 kHz VLIF (Volumetric Laser Induced Fluoresence) Measurements in Turbulent Flows Seeded with Iodine*, in *32nd AIAA Aerodynamic Measurement Technology and Ground Testing Conference*. 2016, American Institute of Aeronautics and Astronautics.

23. Meyer, T.R., Halls, B.R., Jiang, N., Slipchenko, M.N., Roy, S., and Gord, J.R., *High-speed, three-dimensional tomographic laser-induced incandescence imaging of soot volume fraction in turbulent flames.* Optics Express, 2016. **24**(26): p. 29547-29555.

24. Greene, M.L. and Sick, V., *Volume-resolved flame chemiluminescence and laser-induced fluorescence imaging.* Applied Physics B, 2013. **113**(1): p. 87-92.

25. Eckbreth, A.C., *Laser diagnostics for combustion temperature and species*. Vol. 3. 1996: CRC Press.

26. Hiller, B. and Hanson, R., *Properties of the iodine molecule relevant to laser-induced fluorescence experiments in gas flows.* Experiments in Fluids, 1990. **10**(1): p. 1-11.

27. Seitzman, J. and Hanson, R., *Quantitative Fluorescence Imaging: A Comparison of Linear, Predissocia and Saturated Pumping Techniques.* 1992.

28. Steinberg, A.M. and Driscoll, J.F., *Stretch-rate relationships for turbulent premixed combustion LES subgrid models measured using temporally resolved diagnostics.* Combustion and Flame, 2010. **157**(7): p. 1422-1435.

29. Steinberg, A.M. and Driscoll, J.F., *Straining and wrinkling processes during turbulence–premixed flame interaction measured using temporally-resolved diagnostics.* Combustion and Flame, 2009. **156**(12): p. 2285-2306.

30. Filatyev, S.A., Driscoll, J.F., Carter, C.D., and Donbar, J.M., *Measured properties of turbulent premixed flames for model assessment, including burning velocities, stretch rates, and surface densities.* Combustion and Flame, 2005. **141**(1–2): p. 1-21.

31. Ma, L., Wu, Y., Lei, Q., Xu, W., and Carter, C.D., *3D flame topography and curvature measurements at 5 kHz on a premixed turbulent Bunsen flame.*

Combustion and Flame, 2016. **166**: p. 66-75.

32. Carter, C., Hammack, S., and Lee, T., *High-speed planar laser-induced fluorescence of the CH radical using the $C^2\Sigma^+$-$X^2\Pi$(0,0) band.* Applied Physics B, 2014. **116**(3): p. 515-519.

33. Kang, M., Wu, Y., and Ma, L., *Fiber-Based Endoscopes for 3D Combustion Measurements:View Registration and Spatial Resolution.* Combustion and Flame, 2014. **16**(12): p. 3063–3072.

34. Luque, J. and Crosley, D.R., *LIFBASE (version 1.5).* SRI International Report MP, 1999: p. 99-009.

35. Jeffries, J.B., Copeland, R.A., and Crosley, D.R., *Transition probabilities in the $C^2\Sigma^+$-X^2II system of CH.* Journal of Quantitative Spectroscopy and Radiative Transfer, 1987. **37**(5): p. 419-423.

36. Tamura, M., Berg, P.A., Harrington, J.E., Luque, J., Jeffries, J.B., Smith, G.P., and Crosley, D.R., *Collisional Quenching of CH(A), OH(A), and NO(A) in Low Pressure Hydrocarbon Flames.* Combustion and Flame, 1998. **114**(3–4): p. 502-514.

37. Lei, Q., Wu, Y., Xu, W., and Ma, L., *Development and validation of a reconstruction algorithm for three-dimensional nonlinear tomography problems.* Optics Express, 2016. **24**(14): p. 15912-15926.

38. Cai, W., Li, X., Li, F., and Ma, L., *Numerical and experimental validation of a three-dimensional combustion diagnostic based on tomographic chemiluminescence.* Optics Express, 2013. **21**(6): p. 7050-7064.

39. Zhao, Y., Li, X., and Ma, L., *Multidimensional Monte Carlo model for two-photon laser-induced fluorescence and amplified spontaneous emission.* Computer Physics Communications, 2012. **183**(8): p. 1588-1595.

40. Ma, L., Lei, Q., Capil, T., Hammack, S.D., and Carter, C.D., *Direct comparison of two-dimensional and three-dimensional laser-induced fluorescence measurements on highly turbulent flames.* Optics Letters, 2017. **42**(2): p. 267-270.

Chapter 4 Super resolution PLIF demonstrated in turbulent jet flows seeded with I_2

(Manuscript submitted to Optics and Laser Technology)

Wenjiang Xu, Ning Liu, Lin Ma

Abstract

Planar laser induced fluorescence (PLIF) represents an indispensable tool for flow and flame imaging. However, the PLIF technique suffers from limited spatial resolution or blurring in many situations, which restrict its applicability and capability. This work describes a new method, named SR-PLIF (super-resolution PLIF), to overcome these limitations and enhance the capability of PLIF. The method uses PLIF images captured simultaneously from two (or more) orientations to reconstruct a final PLIF image with resolution enhanced or blurring removed. This paper reports the development of the reconstruction algorithm, and the experimental demonstration of the SR-PLIF method both with controlled samples and with turbulent flows seeded with iodine vapor. Using controlled samples with two cameras, the spatial resolution in the best case was improved from 1.3 mm in the projections to 0.04 mm in the SR image, in terms of the spreading width of a sharp edge. With turbulent flows, an image sharpness measure was developed to quantify the spatial resolution, and SR reconstruction with two cameras can improve the spatial resolution by ~2× compared to the projections in terms of the sharpness measure.

Introduction

Planar laser induced fluorescence (PLIF) has been established as a powerful tool for a range of problems [1-8]. However, the PLIF technique suffers from limited spatial resolution or blurring in many situations, which restrict PLIF's capability and applicability. First, the spatial resolution of the current PLIF technique is limited by the imaging optics and the pixel size of the camera. In most flow or flame applications (where microscopic imaging is impractical), the spatial resolution is limited to be on the order of 50 to 200 μm with state-of-the-art imaging optics and camera technologies [9, 10], even though finer resolution is highly desired. Second, blurring can occur due to a variety of reasons to further deteriorate the resolution of the PLIF measurements, such as misalignment of the excitation laser sheet and the focal plane of the camera, mechanical vibration or movement of the experimental rig, and the also the scanning of the laser sheet to obtain PLIF measurements at multiple spatial locations [11, 12]. A straightforward and commonly practiced method to mitigate the blurring issue involves using a small aperture to increase the depth of field (DOF) of the imaging systems, so that a certain range of misalignment, vibration, and scanning can be tolerated and acceptable sharpness of the PLIF images can be maintained [9, 13]. This straightforward approach however is practiced at the cost of signal level, which approximately scales to the second power of the aperture [14].

Under the above understanding, this paper describes an alternative approach to overcome these issues and enhance the spatial resolution of PLIF measurements. The approach is termed super-resolution PLIF, or SR-PLIF. The SR-PLIF technique captures two or more PLIF images simultaneously from different orientations, and then uses these

images to reconstruct a final PLIF image with spatial resolution finer than any of the original images. The SR approach has been extensively investigated under the context of satellite surveillance, video compression, and cartoon rendering [15-17]. This paper reports a new SR algorithm based on tomographic reconstruction, and the combined use of SR and PLIF techniques to enhance the spatial resolution and to remove the blurring of PLIF measurements. Controlled experiments, computation, and demonstration measurements in turbulent flows have been performed to elucidate the feasibility and applicability range of SR-PLIF under the context of flow and flame visualization. It should be noted that the ultimate goal of SR technique is to improve the spatial resolution even when the raw projections are focused. Nevertheless, the work reported here emphasizes the deblurring issue.

Tomographic reconstruction-based super-resolution algorithm

This section describes the mathematical formulation of the tomographic reconstruction-based super resolution algorithm. In conventional SR technique, the observation of LR (low resolution) images are modeled through warping, blurring and subsampling the HR (high resolution) image separately and sequentially, and a sequentially inverse operation is then applied to recover the HR image [18-20]. From modeling perspective, such methods are easy to be understood. Physically, however, the imaging process from HR to LR images is a single process, which means the warping, blurring and subsampling process take role simultaneously. As a contrast, the reconstruction based SR technique described below models the imaging as a single process. The target of this work is to apply tomographic reconstruction on scanning PLIF images from a nitrogen jet flow seeded with iodine molecules, in order to enhance the

spatial resolution and to remove the blurring of PLIF measurements. Using the images (termed projection) taken by two or more cameras, a SR reconstruction was performed to obtain an image with higher resolution. The reconstruction algorithm was based on a tomography algorithm we developed in [21, 22], with certain modifications. The SR reconstruction was mathematically formulated into the following problem:

$$P(x_P, y_P) = \sum_{x_i=1}^{I} \sum_{y_j=1}^{J} \sum_{z_k=1}^{K} SR(x_i, y_j, z_k) \cdot PSF(x_i, y_j, z_k; x_P, y_P) \tag{1}$$

where $P(x_P, y_P)$ represents the value of the measured projections at a pixel located at row x_P and column y_P on the camera chip; *SR* represent the sought super resolution measurement; x_i, y_j, and z_k the *X*, *Y*, and *Z* coordinates of each image element on the *SR* measurements; *I* and *J* the total number of images element in the *X* and *Y* direction of the *SR* measurements; and *K* the total number of image element in the depth direction (set to be 1 in this work since we are studying planar LIF); *PSF* the point spread function defined as the projection formed at (x_P, y_P) by a point source located at (x_i, y_j, z_k) with unity intensity. Noted that the *PSF* does not depend on *SR*. It depends on the lens used in the imaging system and the location and orientation of the imaging system, and it characterizes the distortion, magnification, and blurring associated the imaging systems. In this work, the *PSF* was calculated by a combination of geometrical ray-tracing [23, 24] and a Monte Carlo simulation [25, 26]. In this manner, the warping, blurring and subsampling processes do not need to be modeled individually, as in conventional SR [27]. After the PSF for each camera was obtained, the above equation was solved for SR using the measured Ps (projections) as inputs. The algorithm used to solve Ea. (1) was a modified variation of a tomographic algorithm based on Algebraic Reconstruction Technique (ART) [21, 24, 28].

$$D^I(k) = P(k) - P^I(k) \tag{2}$$

$$SR^{I+1}(l) = SR^{I}(l) + \frac{D^{I}(k)}{\|PSF\|} PSF(k,l) \tag{3}$$

Where I represents the index of iterations, k the index of LR image pixel (when written in lexicographical notation), l the index of SR image. The first step of the iteration, as shown in Eq. (2), calculates the difference between measured projection at the kth pixel and the calculated projection based on the SR obtained in the Ith iteration. The second step then obtains an updated version of SR by correcting the SR from previous step according to Eq. (3). Such correction is performed for all the pixels on the SR image. Above ART solving algorithm is quite similar to the widely used iterative back projection methods in image processing community [29, 30], although the internal observation model is quite different.

Experimental setup

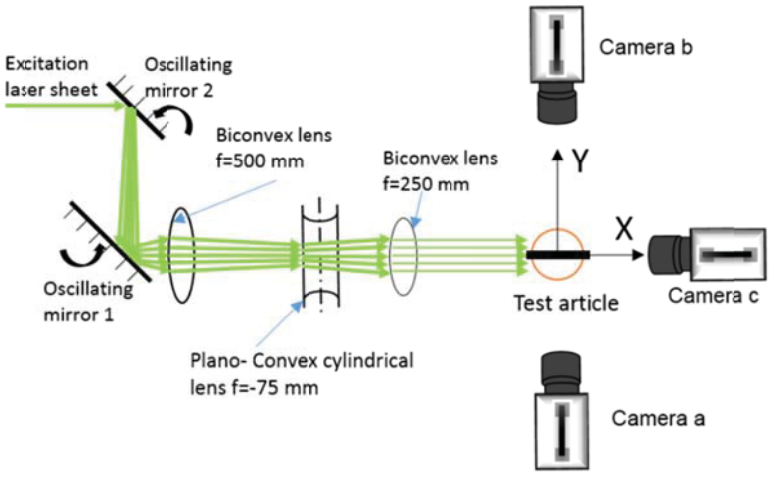

Fig. 4-1. Experimental setup viewed from top

Fig. 4-1 illustrates the experimental setup used in this work. This setup was used to perform two sets of experiments with two different test articles: a controlled test with a

solid target (illustrated by the black bar in Fig. 1) and a demonstration test with a turbulent flow (illustrated by the red circle). The solid sample is a piece of glass plate etched with chessboard pattern with 0.0015 mm precision, as shown in Fig. 2a. The target was mounted on a translational stage, and a coordinate system was defined such that the target plate was in the X-Z plane and the Y axis was normal to the face of the plate as shown. The target was moved in the Y direction by the translational stage with an accuracy of 0.01 mm, and two cameras (shown as camera a and b in Fig. 1) were aligned along the Y axis and used to capture images of the target while it moved. Fig.2a shows an image of the target at Y=2.5 mm taken by camera a, where the target was in sharp focus, to provide a benchmark of the spatial resolution, i.e., the best possible spatial resolution achievable by one camera. The aperture was set to f/2.8 and the magnification ratio was 1.00 at Y=2.5 mm for camera a. Under such condition, the depth of field was estimated to be 0.22 mm based on a 0.02 mm circle of confusion. The magnification was confirmed by matching the physical size of the chessboard patter (9 mm square) to the 450 pixels on camera (each pixel is 20 μm). As the target was moved away from Y=2.5 mm, the images taken by both cameras became out of focus, simulating the issues encountered in practice. As two examples, Fig. 4-2(b) and (c) show two out-of-focus images (hereafter referred to as projections) of the target captured by camera a and b at Y= 6.5 mm, respectively. Fig. 4-2(c) is more blurred than Fig. 4-2(b), because the target moved away from the focus plane of camera b (by 9 mm) more than that of camera a (by 4 mm).

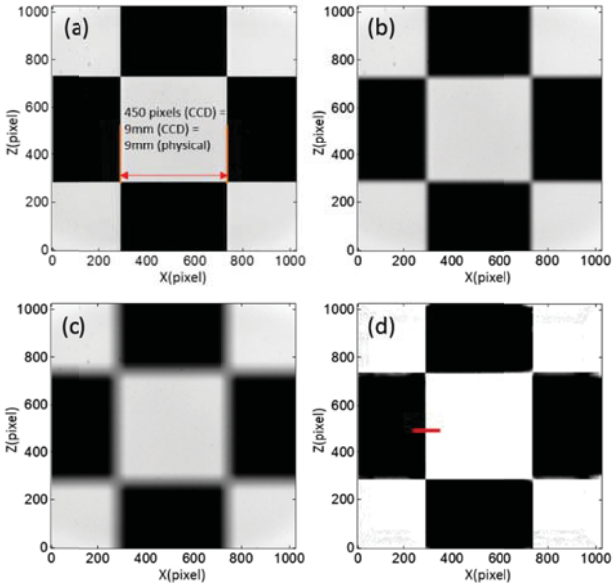

Fig. 4-2. (a): A focused image of the target taken by camera a at Y=2.5 mm. (b) and (c): Out-of-focus image of the target taken by camera a and b, respectively, at Y=6.5 mm. (d): SR image reconstructed from images shown in (b) and (c).

Besides the validation experiments with a controlled target, experiments were performed in turbulent flows, with two major modifications on the experimental arrangement. First, the static target was replaced by a turbulent jet flow. Second, projections at different locations were realized by scanning a laser sheet rapidly across the flow, in contrast to moving the target by a translation stage. In these experiments, the target was replaced by a N_2 (nitrogen) jet flow seeded with ~4% of iodine vapor (I2) by volume. The Reynolds number of the jet was 1,345, and a rod was placed at the exit of the jet to increase turbulent intensity in the flow and also to create more easily recognizable patterns. The flow was then illuminated by an Nd:YLF diode pumped solid state laser as shown in Fig. 1. The laser operated at a repetition rate of 9,280 Hz and generated laser pulses at 527 nm with a pulse energy of ~3 mJ/pulse and a duration of ~300 ns. The output pulses were reflected by two oscillating mirrors driven by two scanners (EOPC SC-30 scanners) as shown in Fig. 1. The laser pulses were then shaped by a series of lens to form thin laser sheets

to excite the I2 vapor in the flow and generate PLIF signals, which were captured by camera a and b simultaneously. By designing the frequencies of the scanners (which oscillated at 1.85 kHz and 5.55 kHz for scanner 1 and 2, respectively), the amplitudes of their oscillations (1:10), and the distance between the mirrors [13, 31], the laser sheet scanned across five different spatial locations between Y=-7.5 to Y=7.5 mm during a period of 0.54 ms. The PLIF images generated by the scanning laser sheet were simultaneously captured by cameras a and b, and will be shown in Fig. 4. A third camera, camera c as shown in Fig. 1, was used in these measurements to monitor the position of the laser sheet experimentally.

Results and discussion

In this section, the SR computation results on both the target experiment and jet flow PLIF measurement are presented. For the target experiment, as seen by visual examination, the SR reconstruction shown in Fig. 4-2(d) substantially improved the resolution compared to either projection. To quantify such improvement, we extracted the width of a sharp edge from the images as shown in Fig. 4-3. Fig. 4-3(a) shows the normalized intensity of images across a sharp edge on the target (in the region illustrated by the red bar shown on Fig. 2(d)). Fig**.** 4-3(a) shows the intensity of a total of 27 images taken by camera a at various Y positions, and the thick violet and green lines corresponded to those extracted from Fig. 4-2(a) and (b), respectively. Based on Fig. 4-3(a), the step width of the sharp edge, defined as the distance in the X direction between the 10% and 90% of maximum intensity [32], was then calculated and used to quantify spatial resolution, as shown in Fig. 4-3(b). The step width of images taken by camera b at various Y locations was also determined and shown in Fig. 4-3(b). As seen from Fig. 4-3(b), the best spatial resolution in terms of the step width was about 0.04 mm for either camera a or b. Note that the

precision of the target was 0.0015 mm, sufficient for calibrating the spatial resolution expected in this work.

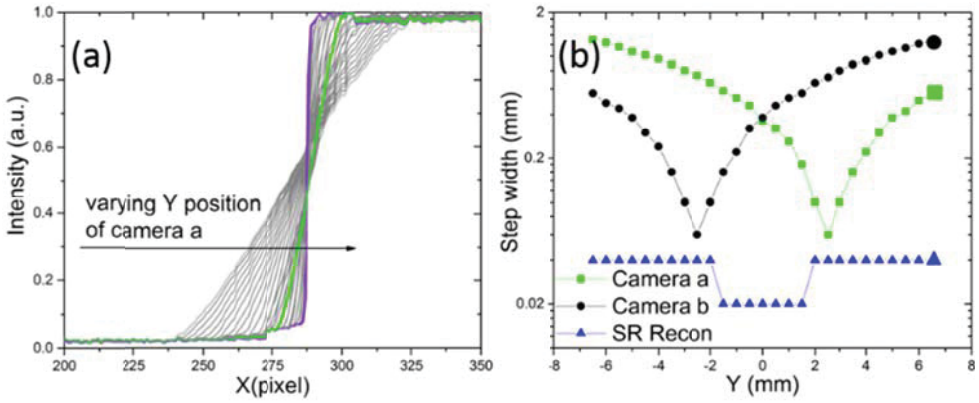

Fig. 4-3. (a) Intensity variation across a sharp edge of projections captured at various positions. (b) Step wide of the projections and SR measurements at various positions.

Finally, Fig. 4-3(b) also displays the step width of the SR measurements based on projections captured by cameras a and b at various Y locations. The data points highlighted by the larger symbols on Fig. 4-3(b) at Y=6.5 mm corresponds to those of Fig. 2(b), (c), and (d). As can be seen, the SR reconstruction was able to provide spatial resolution superior to the projections at all locations. The step of the SR images was ~0.02 mm with projections captured between Y=-2 to 2 mm, and ~0.04 mm with projections captured elsewhere. Such sudden change of the SR resolution between ~0.02 and 0.04 mm was caused by the discrete pixel size used in the SR reconstruction (which was set to be 0.02 mm), and also illustrates the potential of maximizing the SR resolution by optimal choice of the cameras' location.

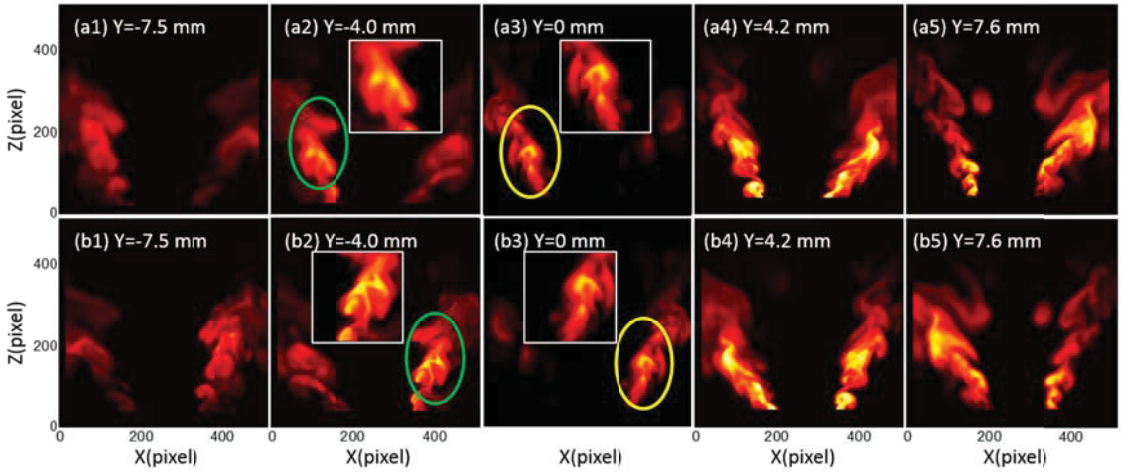

Fig. 4-4. A set of five projections captured by cameras a (top row) and b (bottom row) between Y=-7.5 and 7.5 mm during 0.54 ms.

Since the range of scanning exceeded the focus depth of imaging systems, a common issue encountered in practice to obtain quasi-three dimensional measurements by a planar technique [9, 13]. That is, the PLIF measurements obtained by either one of the cameras exhibited different extent of blurring depending on location of the laser sheet (relative to the focus depth of the cameras). Such blurring is elucidated by the regions highlighted in Fig. 4 with the ovals. These regions corresponded to the same flow feature captured by cameras a and b at the same time (the images' orientations are mirror flipped because the cameras are opposite of each other). When at the cameras were positioned at Y=-4.0 mm, the region (highlighted in the green ovals) was more resolved in the image captured by camera b than a, because the laser sheet was less out of the focal depth of camera b than a at this particular moment. When the cameras were at Y=0 mm, the region (highlighted in the yellow ovals) were equally blurred because the both cameras were equally out of focus. These demonstration measurements were intended to show that the SR technique can be used to ameliorate such blurring and extend the quality and applicability range of the scanning strategy. Note that the white boarded squares in Fig. 4 (a2-a3) and (b2-b3) are zoomed in area of the corresponding ovals, to illustrate the local details clearly.

Before discussing SR reconstruction, we first need to establish an alternative quantitative measure of spatial resolution for turbulent flows. The static target offered the advantage of providing sharp edges so that spatial resolution can be quantified by the step width as describe above. However, there are no such sharp edges available to quantify resolution of turbulent flow measurements as seen from Fig. 4. Therefore, a new measure was needed and this works adopted the concept of image sharpness measure (ISM) as described in [33]. Calculating the ISM involved several steps: the target image was transformed into the Fourier space, the zero frequency point was shifted to the image center, and finally the number of pixels with intensity above a certain threshold was counted in the Fourier space and used as the ISM of the target image. Physically, the ISM concept is based on the observation that for images with higher resolution in the spatial domain, their Fourier transformed images will have modulation transfer function more dispersed in the higher spectral range and higher ISM [32, 33]. In this work, the threshold was set to be one thousandth of the maximum pixel value of the target image following [33].

As a demonstration of the suitability of the ISM, Fig. 4-5 shows the application of the ISM on the static targets. Here the ISM was applied to the projections captured by cameras a and b at various locations (the square and round symbols, respectively), and also the SR reconstructions (the triangle symbols). Comparison between Fig. 5 and Fig. 3b shows that the ISM indeed was able to generate a monotonic correspondence with the step width measure, supporting its use as a measure of resolution for images without clear edges.

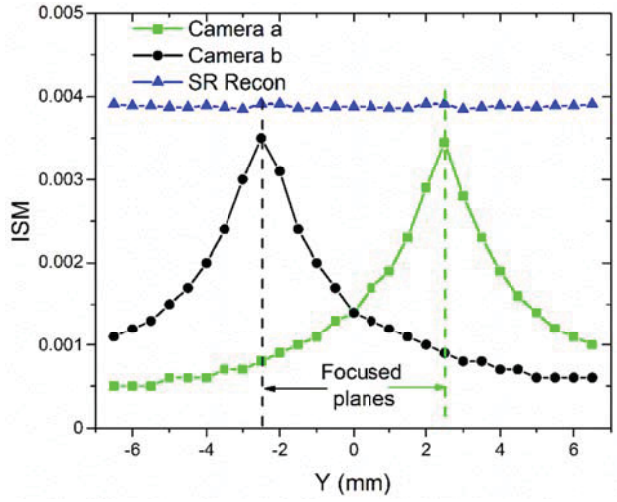

Fig. 4-5. ISM applied to results obtained with the static target.

With the ISM as a measure to quantify resolution, SR reconstruction was performed on the PLIF measurements of the turbulent flow and the results are summarized in Fig. 6. Here, the projections captured by cameras a and be at each Y location were used as inputs to the SR reconstruction. Fig. 6(a) and (b) show sample SR reconstructions obtained using In this section our model is applied to study the forward problem, more specifically, the dependence of the signal level on excitation pulse energy and dimension of the measurement volume (a2), (b2) and (a3), (b3) as the inputs. Visual examination (for example, of the region with the highest I2 concentration in the right branch of the flow) shows that the SR reconstruction resolved the flow better than either of the projections shown in In this section our model is applied to study the forward problem, more specifically, the dependence of the signal level on excitation pulse energy and dimension of the measurement volume (a3) and (b3). The white boarded boxes in Fig. 6(a) and (b) shows more clearly the local details and reveal the effective improvement on the resolution using SR computation, compared with the boxed regions in In this section our model is applied to study the forward problem, more specifically, the dependence of the signal level on

excitation pulse energy and dimension of the measurement volume. The ISM was then applied to the projections and the SR reconstructions, and the results are shown in Fig. 6(c). Several important observations can be made from Fig. 4-6(c). First, the ISMs of the projections (the green square and black round symbols) varied as expected, again confirming the suitability of the ISM for quantifying the spatial resolution. Take camera a (green square symbols) as an example. Its ISM 1) started at a low value at Y=-7.5 mm when camera a was significantly out of focus, 2) gradually increased when camera a became more and more in focus, 3) peaked near Y=4 mm where camera a was closest to its focal plane (shown by the green dotted line), and 4) decreased again when the location of camera a became away from the focal plane. Second, the ISM of the SR reconstruction was consistently higher than that of either the projections, consistent with the visual observation and illustrating the effectiveness of the SR method to ameliorate blurring caused by out-of-focus imaging and to extend the applicability range of the scanning PLIF strategy. Third, the ISMs of the SR reconstructions varied depending on the input projections. The maximum ISM was observed with the projections at Y=0 mm as inputs, illustrating the potential of optimizing the resolution of the SR reconstruction by arranging the cameras' locations carefully. Furthermore, this work used two cameras aligned in opposite orientation, which should not have to be the case. The relative orientations of the cameras can also be adjusted to optimize the resolution of the SR reconstruction.

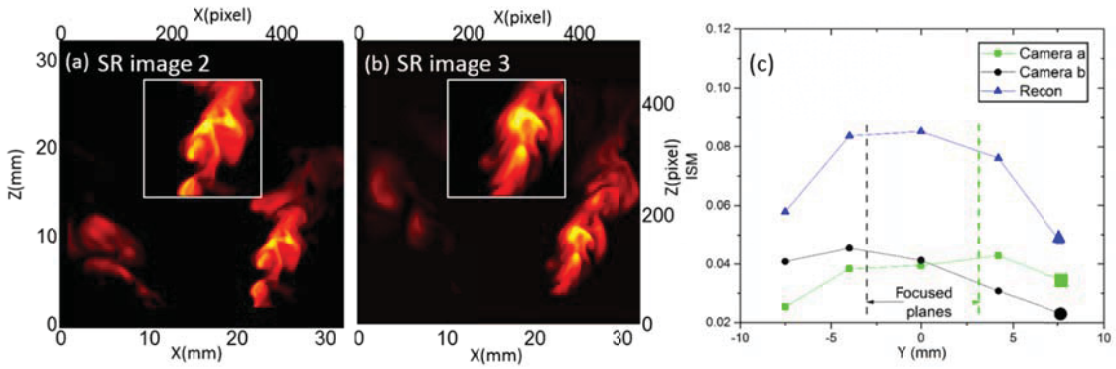

Fig. 4-6. Demonstration of SR-PLIF in turbulent flows. Panel (a): an example SR-PLIF measurement. Panel (b): ISM applied to analyze the resolution of PLIF and SR-PLIF of turbulent flows.

Summary

In summary, this work investigated a new technique to obtain super-resolution PLIF (SR-PLIF) measurements. The SR-PLIF technique used images captured simultaneously from two (or more) orientations to reconstruct a final PLIF image with resolution superior to that achievable by any of the cameras. Proof-of-concept experiments were first conducted with a static target to illustrate the effectiveness of the technique and also to establish a quantitative measure (the ISM) of image resolution. Demonstration experiments were then performed in turbulent flows. These results illustrate the technique's ability to overcome some of the key limitations of traditional PLIF measurements. These results also illustrate the SR-PLIF's potential to expand the capabilities of PLIF measurements, for example, by enhancing the spatial resolution, accommodating misalignment without sacrificing signal level, and obtaining 3D scanning LIF in a wider range.

Acknowledgement

This work is supported by the U.S. Air Force Office of Scientific Research (AFOSR) (grant FA9550-14-1-0386) and the National Science Foundation (NSF, award number 1505112).

References

1. Seitzman, J.M., Kychakoff, G., and Hanson, R.K., *Instantaneous temperature field measurements using planar laser-induced fluorescence.* Optics Letters, 1985. **10**(9): p. 439-441.

2. Lozano, A., Yip, B., and Hanson, R., *Acetone: a tracer for concentration measurements in gaseous flows by planar laser-induced fluorescence.* Experiments in Fluids, 1992. **13**(6): p. 369-376.

3. Miller, J.D., Michael, J.B., Slipchenko, M.N., Roy, S., Meyer, T.R., and Gord, J.R., *Simultaneous high-speed planar imaging of mixture fraction and velocity using a burst-mode laser.* Applied Physics B, 2013. **113**(1): p. 93-97.

4. Paul, P.H. and Najm, H.N., *Planar laser-induced fluorescence imaging of flame heat release rate.* Symposium (International) on Combustion, 1998. **27**(1): p. 43-50.

5. Crimaldi, J. and Koseff, J., *High-resolution measurements of the spatial and temporal scalar structure of a turbulent plume.* Experiments in Fluids, 2001. **31**(1): p. 90-102.

6. Hammack, S.D., Carter, C.D., Gord, J.R., and Lee, T., *Nitric-oxide planar laser-induced fluorescence at 10 kHz in a seeded flow, a plasma discharge, and a flame.* Applied Optics, 2012. **51**(36): p. 8817-8824.

7. Hammack, S., Kostka, S., Lynch, A., Carter, C., and Lee, T., *Simultaneous 10-kHz PLIF and chemiluminescence imaging of OH radicals in a microwave plasma-enhanced flame.* IEEE Transactions on Plasma Science, 2013. **41**(12): p. 3279-3286.

8. Carter, C., Hammack, S., and Lee, T., *High-speed planar laser-induced fluorescence of the CH radical using the* $C^2\,\Sigma^+$-$X^2\Pi$*(0,0) band.* Applied Physics B, 2014. **116**(3): p. 515-519.

9. Cho, K.Y., Satija, A., Pourpoint, T.L., Son, S.F., and Lucht, R.P., *High-repetition-rate three-dimensional OH imaging using scanned planar laser-induced fluorescence system for multiphase combustion.* Applied Optics, 2014. **53**(3): p. 316-326.

10. Foley, C.W., Chterev, I., Seitzman, J., and Lieuwen, T., *High Resolution Particle Image Velocimetry and CH-PLIF Measurements and Analysis of a Shear Layer Stabilized Flame.* Journal of Engineering for Gas Turbines and Power, 2015.

138(3): p. 031603-031603-13.

11. Wilkes, J., Glass, C., Danehy, P., and Nowak, R. *Fluorescence imaging of underexpanded jets and comparison with CFD*. in *44th AIAA Aerospace Sciences Meeting and Exhibit*. 2006.

12. Danehy, P., Bathel, B., Ivey, C., Inman, J., and Jones, S. *NO PLIF study of hypersonic transition over a discrete hemispherical roughness element*. in *47th AIAA Aerospace Sciences Meeting including The New Horizons Forum and Aerospace Exposition*. 2009.

13. Wellander, R., Richter, M., and Aldén, M., *Time-resolved (kHz) 3D imaging of OH PLIF in a flame.* Experiments in Fluids, 2014. **55**(6): p. 1-12.

14. Eckbreth, A.C., *Laser diagnostics for combustion temperature and species, chapter 9*. Vol. 3. 1996: CRC Press.

15. Zhang, H., Yang, Z., Zhang, L., and Shen, H., *Super-resolution reconstruction for multi-angle remote sensing images considering resolution differences.* Remote Sensing, 2014. **6**(1): p. 637-657.

16. Ng, M.K., Shen, H., Lam, E.Y., and Zhang, L., *A total variation regularization based super-resolution reconstruction algorithm for digital video.* EURASIP Journal on Advances in Signal Processing, 2007.

17. Capel, D. and Zisserman, A., *Computer vision applied to super resolution.* IEEE Signal Processing Magazine, 2003. **20**(3): p. 75-86.

18. Humblot, F. and Mohammad-Djafari, A., *Super-resolution using hidden Markov model and Bayesian detection estimation framework.* EURASIP Journal on Advances in Signal Processing, 2006. **2006**(1): p. 036971.

19. Wang, Z. and Qi, F., *Analysis of multiframe super-resolution reconstruction for image anti-aliasing and deblurring.* Image and Vision Computing, 2005. **23**(4): p. 393-404.

20. Wang, Z. and Qi, F., *On ambiguities in super-resolution modeling.* IEEE signal processing letters, 2004. **11**(8): p. 678-681.

21. Cai, W., Li, X., and Ma, L., *Practical aspects of implementing three-dimensional tomography inversion for volumetric flame imaging.* APPLIED OPTICS, 2013. **52**(33): p. 8106-8116.

22. Cai, W., Li, X., Li, F., and Ma, L., *Numerical and experimental validation of a three-dimensional combustion diagnostic based on tomographic chemiluminescence.* Optics Express, 2013. **21**(6): p. 7050-7064.

23. Cai, W. and Ma, L., *Improved Monte Carlo Model for Multiple Scattering Calculations.* Chin. Opt. Lett., 2012. **10**(1): p. 012901.

24. Cai, W., Li, X., Li, F., and Ma, L., *Numerical and experimental validation of a three-dimensional combustion diagnostic based on tomographic chemiluminescence.* Opt. Express, 2013. **21**(6): p. 7050-7064.

25. Zhao, Y., Li, X., and Ma, L., *Multidimensional Monte Carlo Model for Two-photon Laser-induced Fluorescence and Amplified Spontaneous Emission.* Comp. Phys. Comm., 2012. **183**(8): p. 1588-1595.

26. Li, X. and Ma, L., *Effects of Line-narrowing of Amplified Spontaneous Emission Analyzed by a Monte Carlo Model.* J. Quan. Spec. Radi. Trans., 2012. **114**: p. 157-166.

27. Park, S.C., Park, M.K., and Kang, M.G., *Super-resolution image reconstruction: a technical overview.* IEEE signal processing magazine, 2003. **20**(3): p. 21-36.

28. Floyd, J., Geipel, P., and Kempf, A.M., *Computed Tomography of Chemiluminescence (CTC): Instantaneous 3D measurements and Phantom studies of a turbulent opposed jet flame.* Combust. Flame, 2011. **158**(2): p. 376-391.

29. Irani, M. and Peleg, S., *Motion analysis for image enhancement: Resolution, occlusion, and transparency.* Journal of Visual Communication and Image Representation, 1993. **4**(4): p. 324-335.

30. Irani, M. and Peleg, S. *Super resolution from image sequences*. in *Pattern Recognition, 1990. Proceedings., 10th International Conference on*. 1990. IEEE.

31. Wellander, R., Richter, M., and Alden, M., *Time resolved, 3D imaging (4D) of two phase flow at a repetition rate of 1 kHz.* Optics Express, 2011. **19**(22): p. 21508-21514.

32. Smith, S.W., *The scientist and engineer's guide to digital signal processing.* 1997.

33. De, K. and Masilamani, V., *Image sharpness measure for blurred images in frequency domain.* Procedia Engineering, 2013. **64**: p. 149-158.

Chapter 5 Conclusion and future work

This chapter summarizes the dissertation and provides several suggestions for future work.

Conclusion

In summary, this dissertation studied 3D laser diagnostics of turbulent flames and flows using both well-designed experiments and advanced numerical methods. These techniques used cameras, high-speed lasers, and resonant scanners to acquire 2D images of turbulent flows, and used advanced numerical algorithms, such as Algebraic Reconstruction Technique (ART) to predict and reconstruct 3D distribution of key flame and flow properties, such as flame front location, flame front topography, chemical species concentration and so on. The goal of this dissertation thus is to investigate such diagnostics and demonstrate their capability and limitations in a range of turbulent flows/flames. The approaches used in this work to accomplish the goal included both new and well-designed experimental platforms and computational models.

More specifically, chapter 2 reported the measurements of 3D (three-dimensional) flame topography using TC, and its validation by a direct comparison against planar Mie scattering measurements. The results show that the flame topography obtained from tomographic chemiluminescence and the Mie measurement agreed qualitatively (i.e., both methods yielded the same profile of the flame fronts), but quantitative difference on the order of millimeter was observed between these two methods. These results are expected to be useful for understanding the capabilities and limitations of both the 3D tomographic technique and the Mie scattering technique in combustion diagnostics.

To investigate the potential of LIF-based techniques to overcome the limitations

of the TC technique, Chapter 3 reported an analysis of VLIF performance in terms of signal level, size of the field of view (FOV) in 3D, and accuracy. In the VLIF method, the fluorescence signal is generated by a laser slab with a certain thickness (ranging from several millimeters to several centimeters in our group's work) and is recorded by cameras from different perspectives. The VLIF method enables study on any particular area of interest and on either reacting or non-reacting flows. Both experimental and computational studies were conducted in this work to analyze the performance metrics of VLIF. Comparison of the model simulation with experiment validated the VLIF model, and the results show that the reconstruction accuracy of VLIF technique improves with the pulse energy.

The above tomographic 3D measurement techniques, either TC or VLIF, have limited spatial resolution in a given measurement volume (or vice versa, limited measurement volume under a given spatial resolution), constrained by the number of cameras used in the experiment. Chapter 4 therefore describes the development and demonstration of a new method, named SR-PLIF (super-resolution PLIF) to overcome these limitations. The method uses PLIF images captured simultaneously from two (or more) orientations to reconstruct a final PLIF image with resolution enhanced or blurring removed. This method is useful when high resolution flow details in a particular plane is desired, while the high resolution in all three directions is difficult to achieve. Moreover, it is useful to extend the measurement volume of scanning 3D diagnostics. Using controlled samples with two cameras, the spatial resolution in the best case was improved from 1.3 mm in the projections to 0.04 mm in the SR image, in terms of the spreading width of a sharp edge. With turbulent flows, an image sharpness measure was developed

to quantify the spatial resolution, and SR reconstruction with two cameras can improve the spatial resolution by ~2× compared to the projections in terms of the sharpness measure.

Future work

The work performed in this dissertation also help to identify the flowing research directions for future work:

1) The demonstration of VLIF measurements in highly turbulent flames to obtain fundamental flame properties. This work studied turbulent flames with turbulent Reynolds number up to 5,000 in a volume up to ~5 cm× 5 cm×5 cm. Turbulent flames encountered in practice are of larger scale, higher Reynolds number, and also higher turbulence level. Three-dimensional measurements and three-dimensional flame statistics are solely needed for such flames. However, performing multi-view and 3D tomographic measurements on such flames is both of great interest and significant challenge. Experimentally, limited optical access, field-of-depth of the imaging system, spatiotemporal resolution requirements are all significant challenges. Numerically, it is quite computationally expensive to solve a large tomography system with inputs acquired from many perspectives and at high speed. Despite all the challenges, it is worthwhile to investigate the feasibility of such measurements given the scientific significance of the data. Furthermore, the continuing development of laser, camera, and fiber technologies should substantially reduce the implementation difficulties.

2) Extension of the tomographic techniques to measurements of multi-scalars and vector fields. The techniques reported in this dissertation are targeted on one single properties, such as flame topography or a single species concentration, therefore only a single aspect

of the turbulent flame can be studied. Both for scientific study and engineering applications, measurements of multiple properties simultaneously are also in desired. For example, the study of fundamental turbulent-chemistry interactions requires information of both turbulence (e.g., velocity field) and the concentration of a range of chemical species. Multidimensional measurements of flow velocity field and two or more chemical species simultaneously can be significant contribution to enhance the understanding of turbulent flame dynamics. One possibility involves the simultaneous application VPIV [1, 2] and VLIF [3] measurement. Again, such measurements would encounter significant practical challenges, and the continued hardware advancements would help to mitigate such challenges and to facilitate the implementation of the measurements.

References

1. Elsinga, G.E., Scarano, F., Wieneke, B., and van Oudheusden, B.W., *Tomographic particle image velocimetry.* Experiments in fluids, 2006. **41**(6): p. 933-947.

2. Tokgoz, S., Elsinga, G.E., Delfos, R., and Westerweel, J., *Spatial resolution and dissipation rate estimation in Taylor--Couette flow for tomographic PIV*. Experiments in fluids, 2012. **53**(3): p. 561-583.

3. Wu, Y., Xu, W., Lei, Q., and Ma, L., *Single-shot volumetric laser induced fluorescence (VLIF) measurements in turbulent flows seeded with iodine.* Optics Express, 2015. **23**(26): p. 33408-33418.